Yeganeh M, Shahtahmasebi N, Kompany A, Karimipour M, Razavi F, Nasralla NHS, Siller L.

The magnetic characterization of Fe doped TiO2 semiconducting oxide nanoparticles synthesized by sol–gel method.

***Physica B: Condensed Matter* 2017**

DOI: http://dx.doi.org/10.1016/j.physb.2017.02.010

The magnetic characterization of Fe doped TiO_2 semiconducting oxide nanoparticles synthesized by sol–gel method

M. Yeganeh [a,*] ,N. Shahtahmasebi [b], A. Kompany [b], M. Karimipour [c], F. Razavi [d], N. H. S. Nasralla [e], L. Šiller [f]

[a] Department of Physics, Kosar University of Bojnord, Iran, P. O. Box 94104455

[b] Department of Physics, Ferdowsi University of Mashhad, Iran

[c] Department of Physics, Vali-e-Asr University of Rafsanjan, Iran

[d] Department of Physics, Brock University, Canada

[e] Electron Microscope and Thin Film Department, Physics Division. 33 El Buhouth st., Dokki, 12622 Giza, Egypt

[f] School of Chemical Engineering and Advanced Materials, Newcastle University, NE1 7RU, UK

[*] Corresponding author: Dr. Mahboubeh Yeganeh at Department of Physics, Kosar University of Bojnord, Iran. P. O. Box 94104455. Phone:+98 058 322 62861, Fax:+98 058 324 27408, mahboubeh.yeganeh@yahoo.co.uk

Abstract

In this work Fe doped TiO_2 nanoparticles were synthesized at different Fe/Ti molar ratio from 1% to 5% by sol-gel technique. The post annealing of the samples was carried out at T= 400, 600, and 800 $^\circ$C. HRTEM of the samples revealed that the mean size of the nanoparticles increases from about 8 nm to about 100 nm as the annealing temperature increased. SQUID magnetometry of 1% and 5% Fe doped TiO_2 has shown mixed ferromagnetic and paramagnetic phases within the crystal while ferromagnetic order with T_c about 350 K was only observed in 5% Fe:TiO_2 sample annealed at T=800^o C**.** The oxygen vacancy mediated ferromagnetic (FM) interaction could be responsible for the observed FM.

Keywords: Nanoparticles, Fe doped TiO_2, Sol-gel, Magnetic properties, SQUID

1. Introduction

Functional properties of TiO_2 can be improved by a small amount of doping, and elements such Fe, Nb, Ta, V, Al, H, Cr, Zr and Ca are frequently used as dopants [1]. Since the radius of Fe^{3+} (0.64 Å) is similar to that of Ti^{4+} (0.68 Å), and Fe^{3+} might easily be incorporated within the crystal lattice of TiO_2, iron has been considered to be an appropriate candidate for doping [2]. In fact there is much interest in Fe-doped TiO_2 as it has potential applications in spintronic and magneto-optic devices [3, 4].

Room temperature ferromagnetism in Co:TiO_2 (anatase) has been observed by Matsumoto et al. [3] and this opened up a new research activity in transition metal doped TiO_2 and other oxides. Giant magnetic moments have been observed by Orlov et al. [5] in dilute semiconductor titanium oxides thin film doped with Co and Fe. The origin of ferromagnetism in iron implanted rutile single crystals were also investigated by conversion electron Mössbauer spectroscopy (CEMS), zero-field-cooled (ZFC) and field cooled (FC) SQUID measurements [6].

Transition metal doped TiO_2 crystals have been prepared through many techniques: wet chemical synthesis [7], sol–gel method [8], thermal hydrolysis [9], sonochemical route [10], thermal plasma synthesis by DC plasma jet using $TiCl_4$ and iron (III) acetylacetonate as precursor [11], RF plasma synthesis from metal mixtures [12] and oxidative pyrolysis of organometallic precursors in induction thermal plasma [13, 14], ion-implantation [15], ion beam induced chemical vapor deposition (IBICVD) [16] and oxidative pyrolysis of liquid-feed metallorganic precursors in a radiation-frequency (RF) thermal plasma [13, 17].

Wang et al. [18] prepared Fe(III)-doped TiO_2 nanoparticles by hydrothermal method to investigate the photo-electrochemical behaviors of the particles when Fe(III) content was as low as 0.5%. Chen et al. [19] produced nanocrystalline Fe-doped TiO_2 with size of 60 -70 nm by a sol-gel technique to study the photocatalytic properties and the optimum content of Fe-doped was 0.05% (mass fraction).

The structural investigations on TiO_2 and Fe-doped TiO_2 nanoparticles synthesized by laser pyrolysis at Fe/Ti atomic ratio of 0.07, 0.15 and 0.25 were performed by Alexandrescu et. al. [13]. The photocatalytic activity of a sample of Fe doped TiO_2 nanoparticle synthesized by hydrothermal method were investigated by Jeong et al. [20]. The magnetic properties of Fe-doped TiO_2 milled in different milling atmospheres were studied by Lin et al. [21]. The Fe concentration was 4.468, 4.227 and 4.473 at% for the powders milled in argon, air and oxygen, respectively. However, they did not mention the size of the particles, but the VSM measurements showed the ferromagnetic behaviors for all the samples at room temperature with the enhanced magnetism as the concentration of oxygen vacancies increased (i.e. particle milled in Ar). Rodr´ıguez-Torres et al. [22] prepared Fe doped TiO_2 anatase-type nanoparticles at 2.8 and 5.4 at.% Fe by micro emulsion method and they concluded that while the samples have two magnetic component of paramagnetic Fe^{3+} ions and antiferromagnetically coupled Fe^{3+}, but do not show the ferromagnetic order.

The nanocrystalline Fe-doped TiO_2 powders were prepared by Ma et al. [23] through a hydrothermal method to consider the photocatalytic activity of the powder. The Fe/Ti ratio was Fe/Ti = 1, 2, 3, 4, 5 at. %. The magnetic properties of nanoparticle iron-doped anatase TiO_2 were measured by Melghit et al. [24]. They estimated the amount of Fe in their prepared sample to be about 17 at% using the EDAX data taken at a number of selected areas throughout the sample. Their sample had a

superparamagnetic state with a possibility of antiferromagnetism at low temperatures. Karimipour et al [25] were also investigated the magnetic properties of Ni-doped TiO_2 nanoparticles synthesized by sol-gel method and the presence of ferro-magnetic and antiferromagnetic interactions were observed in their samples. Carisan et al. [26] produced iron-doped TiO_2 nanopowder at 0, 0.5, 1, 2 and 5 wt% of Fe/Ti ratio by sol-gel technique to investigate the photocatalytic activity. They also measured room temperature magnetic susceptibility of the samples by VSM system and found that while the undoped TiO_2 sample was diamagnetic, the doped samples were paramagnetic. Oganisian et al. [27] studied magnetic properties of TiO2 powders doped with 1, 5 and 10 mol% Fe prepared by sol-gel method . The post annealing temperature of their samples was 500^o C and the particles size were in the range 200–350 nm. They found that the sample with 1% Fe content has superparamagnetic dependence of magnetization, while the samples at 5 and 10% Fe revealed the paramagnetic behavior with the negative Weiss constant.

In this work, the Fe doped TiO_2 nanoparticles have been prepared at a wide variety of Fe/Ti molar ratio (1%, 3%, and 5%). The post annealing of the samples were taken place at different temperatures from 400°C to 800°C. It is desired to produce a sample with ferromagnetic order with a Curie temperature above room temperature. The advantage of this preparation technique is while the concentration of dopant can be controlled, the post annealing can be done at different ambient temperatures to tune the amount of oxygen vacancies in the prepared powder. Lin et al [21] found that by increasing the oxygen vacancies the magnetism of the sample increases. Shimizu et al. [28] were also achieved the same results for the single crystal of Ni doped TiO_2 in which samples with less oxidic conditions shown stronger

magnetic behaviors. In this work we study the effect of post annealing in air on the magnetization of Fe-doped TiO_2.

2. Experimental procedure

2.1. Synthesis of Fe doped TiO_2 nano-powders

A nano-powder of Fe doped TiO_2 was synthesized by the sol-gel method at different Ti/Fe mole ratio (1%, 3%, and 5%). The initial sol consists of Iron (III) Chloride 6-Hydrate, $C_{12}H_{28}O_4Ti$ (Tetraisopropyl orthotitanate), ethanol, citrate acid and $C_5H_8O_2$ (Acetyl acetone). The sol was stirred and dissolved at 40 °C and then was refluxed at T=120 °C for 6 h. The development of polymerization and evaporation of the solvent achieved by further slowly heating of the resulting mixture at T= 80 °C for 14 h in an open bath until a brown wet gel was obtained. Heating at this temperature causes the polymerization between citrate acid, acetyl acetone and complexes, and finally sol becomes more viscous as a wet gel. Finally, the wet gel is fully dried by direct heating on the hot plate at T=150 °C for 1 h. The resulting product is a black-brown porous gel as aerogel. Then the aerogel is ground to produce a precursor powder which is then post annealed at 400, 600 and 800 °C for 1 h (in air) and cooled down to room temperature.

2.2. Characterization of powders

The crystalline structure of the prepared powder at different doping concentrations and different annealing temperatures were examined by X-ray diffraction (XRD) analysis utilizing a D8 Advance Bruker system using CuKα1 (λ=0.154056 nm) radiation and 2θ varying from 20° to 70°. JEOL 2100F field

emission gun transmission electron microscope (FEG TEM) operating at 200 keV is used to record HRTEM micrographs and electron diffraction patterns of the prepared nanopowders. The Fe doped TiO_2 nanopowders dispersed onto a holey carbon grid in order to be prepared for HRTEM analysis. A GATAN Tridiem spectrometer was used to extract chemical information from the same region as the diffraction pattern through electron energy loss spectroscopy (EELS).

High-resolution X-ray photoemission spectroscopy is performed at the National Centre for Electron Spectroscopy and Surface Analysis (NCESS), Daresbury Laboratory, UK with a rotating anode Al $K\alpha$ ($h\upsilon$ =1486.6 eV) X-ray source, a 7 crystal X-ray monochromator and a 300 mm mean radius spherical sector electron energy analyzer (Scienta ESCA 300) with parallel electron detection system. The measurements were carried out at the 10^{-9} Torr.

The magnetic behavior of the samples has been investigated by superconducting quantum interference device (SQUID) magnetometry. The noise level is as low a 10^{-8} emu. The superconducting magnet, detection coils and SQUID are cooled to cryogenic temperatures by utilizing liquid helium. The magnetometer allows high sensitivity field cooling and zero field cooling experiments to be made in the temperature range 2K to 400 K.

3. Results and discussion

The XRD patterns of prepared nanoparticles at different doping concentrations and different annealing temperatures are shown in Fig. 1. The Fe doped TiO_2 nano-powders annealed at T=400 ^{o}C show both anatase and rutile structure with the dominance of anatase structure (see Fig. 1(a,d)). While the annealing temperature is increased to 600 ^{o}C the rutile phase becomes dominant over anatase phase (see Fig.1

(b,e)) and annealing temperature at T=800 ^{o} C causes the disappearance of the anatase structure and the samples show monostructure rutile phase (see figure 1(c,f)).

The diffraction peaks of iron or iron compounds such as Fe_2O_3 or Fe:TiO can not be observed which suggests the formation of an iron-titanium solid solution, where the Fe^{3+} is incorporated into the TiO_2 crystal structure substitutionally due to similar ionic radii (Ti (0.68 Å) and Fe (0.64 Å)). X-ray diffraction measurements also revealed that by increasing the temperature and the iron concentration, the TiO_2 phase changes from anatase to rutile crystal structure.

The phase contents of the powders were determined using Spurr and Myers method [29] according to the following equation:

$$X_A = 1\text{-}X_R = (1+1.26 * I_{27.5}/I_{25.3})^{-1}$$

Where the subscripts (A) and (R) represent anatase and rutile respectively. $I_{27.5}$ and $I_{25.3}$ are the relative intensities of the rutile (110) peak at 2θ ~27.5° and the anatase (101) at 2θ ~25.3°. The results were summarized in table 1 and it can be found that the rutile phase quantity is increased by increasing the annealing temperatures from 400 °C to 800°C in agreement with previous literature [30-32] and as increasing the dopant concentrations from 1% to 5% the rutile content has increased.

The crystallite size value is calculated from Williamson and Hall (W-H) method [33, 34] which accounts broadening of the diffraction lines due to crystallite size and lattice strain. The latter is arising from crystal imperfection and the distortion of the regular lattice [35].

In the W-H method, it is assumed that the size broadening and strain broadening are independent of each other. i.e.

$$\Delta_{hkl} = \Delta_{\Lambda} + \Delta_{\varepsilon} = \left[K\lambda / \Lambda \cos\theta_{hkl}\right] + \left[4\varepsilon \tan\theta_{hkl}\right]$$

and, $\Delta_{hkl}\cos\theta_{hkl} = [K\lambda/\Lambda] + [4\varepsilon\sin\theta_{hkl}]$ is the Williamson-Hall equation. The crystallite size is obtained from the intersection of the linear fit of the value of $\Delta_{hkl}\cos\theta_{hkl}$ as a function of $4\sin\theta_{hkl}$ and the lattice strain ε is obtained from the slope of the fit. The results are summarised in table 1. As reported by Choudhury et al. [36] by increasing the annealing temperatures, crystallite sizes are increased and cause the release of lattice strain [36].

According to the table 1 the lattice strain is positive for the 1% dopant annealed at 400 and 600 °C and 5% annealed at 400 °C, indicating the tensile strain. Ti is 6 fold coordinated in anatase and rutile structures. Each titanium is bonded to 6 oxygen and each oxygen is bonded to 3 titanium while the anatase has more distorted structure than rutile. It means two of the titanium-oxygen bonds are much longer than the rest. Also the O–Ti–O bond angles deviates more from 90° in anatase in comparison to rutile. Therefore, by increasing the annealing temperature and phase transformation to rutile, the lattice strain decreases. As can be observed the lattice strain of the samples in this work is reduced by increasing the size of the crystallite and phase transformation to rutile. In 1% Fe dope TiO_2 annealed at 800 °C, in which the phase composition are totally rutile (see table 1) the lattice strain is negative indicating compressive strain. The negative strain were also observed in nanoparticles of TiO_2 annealed at high temperature [37-39]. As described in table 1 by increasing Fe concentration, the anatase to rutile transformation is facilitated and this can cause the negative lattice strain for the 5% Fe sample annealed at 600 °C. By increasing the annealing temperature of 5% Fe doped sample to 800 °C, the lattice strain increases, which can be explained by the increasing the oxygen vacancies created by dopants at high temperature. This has been suggested by Diebold [40] who showed that the

annealing at high temperature in UHV reduces the TiO_2 surface and creates point defects and following the donor-like surface defect states. Choudhury et al. [41] also observed that the significant amount of oxygen vacancies are created in vacuum annealed Fe doped TiO_2 nanoparticles.

The TEM images and the selected area electron diffraction (SAED) patterns of nano-particles at 1 and 5% Fe dopant and annealed at different temperatures were shown in Figs. 2 and 3. The SAED patterns illustrate a set of halo-rings and discrete spots corresponding to poly-crystalline structure of the prepared nano-particles. As the annealing temperature was increased, the electron diffraction patterns are sharper and the spots become more distinguishable. From TEM results, it can be seen that the samples annealed at 400^{o} C are in particle size ranges from 6 to 11 nm. The particle size of the samples is increased from 22 to 30 nm upon annealing at 600^{o} C and from 50 to 100 nm upon annealing at 800^{o} C.

Banfield et al. [42-44] found that the prepared TiO_2 nanoparticles had anatase and /or brookite structures, which is transformed to rutile after reaching a certain particle size; once the rutile phase was formed, it grew much faster than anatase structure. Zhang and Banfield [42, 44] established that for equally sized nanoparticles, the anatase phase was thermodynamically stable for sizes <11nm, brookite structure was stable for sizes between 11 and 35nm, and rutile phase was stable for sizes> 35nm. Therefore, the present results agree to the ones reported by Banfield et al. [42-44] in which the anatase phase is the dominant and stable phase when the particle size ranges from 6-11nm but from particle size of 50nm the rutile phase is the most dominant phase.

It has been shown by Li et al. [45] that anatase to rutile phase transformation only occurred in the temperature range from 973 to 1073K and the particle size of

both anatase and rutile phases increases as the temperature increases, but the growth rate is different and the rutile phase has a much higher growth rate than anatase phase. The anatase type to rutile type transformation after doping by iron is accelerated and shifted the transformation to lower temperature [9], which confirms our results in which the transformation of anatase to rutile phase has occurred at 600 ^{o}C by doping TiO_2 with 5% of Fe.

The EELS spectrum of the above samples is shown in Fig. 4. In EELS, titanium 2*p* electron is exited to the unoccupied state which is the lower unoccupied 3*d* state at threshold energy (the obtained spectra is due to the spin–orbit splitting into $2p_{3/2}$ (L_3) and $2p_{1/2}$ (L_2) levels, with a separation of 5.4 eV [46]). In general, four peaks (two doublets) were observed in literature [47] where the double peaks at lower energy loss comprises the Ti L_3 edge and the second ones at higher energy loss the Ti L_2 edge.

The molecular-orbital energy-level diagram for the Ti oxides is discussed in ref [47]. The interaction between the Ti 3*d* and oxygen 2*p* orbital causes the $2e_g$, $1t_{2g}$, $2t_{2g}$, and $3e_g$ MO levels, in which the $2e_g$, $1t_{2g}$ are bonding and the latter two are anti-bonding orbitals [48] and the σ bonds are due to the e_g orbital while the π bonds from t_{2g} orbitals. Also all levels placed below $2t_{2g}$ level are completely filled with electrons. As mentioned before the Ti $L_{3,2}$ lines are due to the transitions from the inner Ti 2*p* levels to the titanium 3*d* levels which the *L*3 edge is due to transitions from $2p_{3/2}$ Ti level to the $2t_{2g}$ MO level and the peak *b*, which is due to transitions from the $2p_{3/2}$ Ti level to the $3e_g$ MO level [49] (the peak *a* and *b* [47] in table 2). In Fig.4 the peak *a* and *b* and also *c* and *d* reported in [47] can not be distinguished due to limited instrumental resolution, but the Ti L_3 and L_2 edge are observed at 458 and

463 eV, respectively for 1% Fe doped TiO_2 annealed at 400^o C and at 461 and 466 eV for 5% Fe:TiO_2.(See table 2) which are in agreement to results in ref [47] .

The O *K* edge consists two parts as reported [47]. The first part which is in the energy region between 529 eV and 535 eV (Peak labeled by A which is assigned to O2*p* → Ti 3*d*(t_{2g}) and B to O 2*p* → Ti 3*d*(e_g) in table 2 [47]) originated from transitions between oxygen 1*s* and 2*p* σ* states that are hybridized with empty Ti 3*d* orbitals [50].

The second set of bands are due to transitions from oxygen 2*p* states that are hybridized with Ti 4*s* and 4*p* states [50] (presence of the peaks C, D, and E in table 2). A very small peak appeared in the Fe 5% doped TiO_2 annealed at 600°C (and also at T=400°C) at energy~708 eV which is due to the L_3 absorption edge of Fe. As can be seen in table 4 the energy position of EELS spectrum of our sample are in good agreement with energy position reported by Stoyanov et al. [47] and references in there by considering the of energy resolution limitation in our studies.

The XPS spectra of Fe 2p of the 1% Fe and 5% Fe annealed at 800^o C are presented in figure 5. Curve fittings for these samples are based on a critical evaluation of the existing literatures and considering the multiplet splitting, surface and satellite structure contributions and the use of the doublet functions to fit Fe 2p spectra [51-54].

The Fe 2p spectrum of the 5% annealed at 400 ^{o} C was reported in our previous work [55]. As it can be seen in figure 5, the Fe ions are in mixed valence (Fe^{2+} and Fe^{3+}) states, while at the surfaces of the nanoparticles, the Fe^{3+} ions are dominant. The observed spectra significantly different from the Fe 2p spectra of the metallic Fe in which the contribution of the metallic peaks in TiO_2 is at around 707 eV [56, 57].

In Fe 2p spectra, the $2p_{3/2}$ peak exhibits an asymmetric tail at higher binding energy. This tail is assigned to the surface structures, which have different binding energies compared to that of the bulk structure [58]. The reason for this high-binding energy tail can be due to the decreased crystal field energy for the Fe-ions located at the surface (top two atomic layers) compared to those located within the bulk [59] (i.e. the coordination number for atoms in the surface is less than the number of atoms in the bulk). Therefore, the energy of the core levels of the surface atoms is different from that in the bulk. This is especially true in the case of high resolution XPS, as the volume contained in the first surface layer can be responsible for roughly half of the photoelectron signal, and even when the shift between the bulk and the surface is small it can be detected [60].

Figure 6 present the Ti 2p of the 5% Fe annealed at different temperature. The Ti 2p XPS peak position of the 1% and 5% are summarized in table 3. It is noted that by increasing the annealing temperatures and the iron concentrations, the Ti 2p spectra of all Fe doped TiO_2 nanoparticle samples have small peak shifts to lower binding energy shift. The same trend was observed in the ferromagnetism study of doped and undoped TiO_2 by Santra et al. [56]. They attributed this negative shift to increasing amount of oxygen vacancy upon annealing and Fe^{3+} substitution to Ti^{4+} lattice site. In fact, by Fe^{3+} substitution to Ti^{4+} lattice site, additional oxygen vacancies are created to maintain the charge neutrality in the host TiO_2 crystal. These results are consistent with XRD data that show that by changing the calcination temperature and the iron concentration the crystal phase and crystallite size are changed.

Figures 7 (A)-(D) shows the variation of magnetization as a function of external magnetic field *H* in the range 0–50 kOe for the 1% and 5% Fe doped TiO_2

annealed at T=400ºC and 800 ºC and the magnetic characterization were measured at 5K.

At first glance it seems that the hysteresis loops measured at 5 K in Fig. 7 show the paramagnetic or superparamagnetic behavior of the material, but the enlarged hysteresis loops near the origin in insets of Fig .7 (A) and (B) (and also in table 4), show that, when the applied field is reduced to zero, a small component of remanent magnetization still exists in these samples. A coercive field should be applied in order to have the zero magnetization. Since the soft magnets may have a hysteresis loop with a very small area, it may be concluded that the measured samples exhibit some evidence of ferromagnetic behavior.

The experimental M-H curves obtained at 5 K were fitted by utilizing the theory of the magnetism of the local moments:

$$M = NgJ\mu_B B_J(x)$$

in which *N*, g, *J*, and μ_B are the number of magnetic ions per gram, the Lande factor, total quantum number, and the Bohr magneton, respectively. $B_J(x)$ is the Brillouin function, where $x = gJ\mu_B H / k_B T$. The results were shown in figure 7 (C) and (D) and, in the case of the 1% Fe:TiO_2 annealed at T=400ºC, a good description of the data is obtained with the local moment Brillouin function and an effective magnetic moment of ~4.9 μ_B being obtained. Such a value is very close to the 5 μ_B expected for isolated paramagnetic Fe^{3+} ions. Similar fits to the M-H curves of 1% Fe:TiO_2 annealed at 800º C and 5% Fe:TiO_2 annealed at T=400 º C were less successful but yielded effective magnetic moments of ~ 2.9, 3.2 μ_B respectively. The field-dependent magnetization curve of the 5% Fe:TiO_2 annealed at T=800 º C had the

poorest agreement with the isolated paramagnetic ion model, the fitted effective magnetic moment of ~ 1.1 μ_B not correctly describing the nature of this material.

The magnetization versus field plot measured at room temperature has been illustrated in Fig. 8. The magnetization data of the 5% Fe:TiO_2, annealed at 800ºC, recorded at 5K and 300K, were plotted as function of H/T as shown in Fig 9. The enlargement of the hysteresis loop near the origin in the inset of Fig 9 represent that there is still a big coercivity field ~370 Oe (see also table 4) at room temperature. Also, the fact that the magnetization data at two different temperatures do not appear to overlap on the H/T plot suggests the simple model of non-interacting paramagnetic or superparamagnetic magnetic system is not applicable to 5% Fe:TiO_2, annealed at 800ºC. Also, it can be observed that the value of the magnetization is reduced at higher annealing temperature (T=800° C) compared to the annealing at T=400° C.

Temperature dependence of magnetization was measured from 5 to 350 K in regimes zero-field-cooled (ZFC) and field-cooled (FC) in applied dc field of 25 Oe.

The ZFC and FC curves of 1% Fe doped TiO_2 annealed at T=600º and 800º C have been shown in Fig 10. (a) and (b) (inset). While the FC curve of the sample annealed at T=600º C almost has coincided to ZFC curve for this sample, post-annealing at 800 °C (Fig. 10 (b)) leads to slight divergence of the FC and ZFC curves. The same behavior was observed for the ZFC and FC curves of the 5% Fe doped TiO_2 annealed at T=600ºC (Fig. 10 (c) (inset)). The ZFC and FC curves of this sample deviate around 350 K. Akdogan et al. [61] observed almost the same feature in the ZFC and FC curves of the low doses of Co-implanted TiO_2 rutile and they attributed this rather unusual behavior to the coexistence of a weak ferromagnetic and a superparamagnetic phase.

The prepared 5% Fe doped TiO_2 and annealed at T=800^{o}C exhibited a steady drop in magnetic moment with increase in temperature, indicating magnetic order (Fig 10. (d)). These results can be explained by the fact that the precipitates become larger at higher post-annealing temperature [62]. As it can be seen the ZFC and FC curves of this sample are close together. Akdogan et al. [61] attributed this progression to the dominance of ferromagnetic phase in this sample.

It can be seen that all of the samples have additional paramagnetic components at low temperatures in which magnetization curves rapidly increases with decreasing temperature showing the paramagnetic behavior (Fig 10), with a $1/T$ -like temperature dependence. It has been suggested by Shimizu et al. [28] that in these cases the two phases with the same crystal structure may be mixed.

As a result, it is considered that the magnetization does not saturate even at 5 K because of a considerable high field magnetic susceptibility and as it was mentioned before, this behavior as well as the increasing behavior of magnetization at low temperatures reveals that there may be paramagnetic component coexisting with ferromagnetic phase [28]. It is also interesting if one compares the magnetization of these samples to those reported recently by Melghit et al. [24]. They could achieved a maximum of magnetization of the sample at 12 kOe about 0.00015 (emu/g) at room temperature while the 5% Fe doped TiO_2 annealed at T=800°C has shown the magnetization of about 0.02 (emu/g) with the same parameters (field=12 kOe and room temperature).

In order to investigate the interactions among the Fe moments we have plotted the $(M/H)^{-1}$ or reciprocal of the susceptibility against temperature by using the data obtained in FC curves (see figure 11 (a, b, c, d)). The linear, high temperature, fit curve illustrates the deviations from the Curie-Weiss law at lower temperatures.

Extrapolation of the linear fits to zero achieved at about -55, -233, and -250 K for the 1% Fe:TiO_2 annealed at T=400 and 800^o C and 5% Fe:TiO_2 annealed at T=600 ^{o} C, respectively. The negative values of the Curie-Weiss temperature, θ, is an indication of the antiferromagnetic behavior of the interactions between the magnetic entities which its strength increases with the doping level as it was observed in [22], and also as the post annealing temperature is increased.

The fact that the samples of 1% Fe:TiO_2 annealed at T=400 and 800^o C and 5% Fe:TiO_2 annealed at T=600 ^{o} C exhibit a $(M/H)^{-1}$ response which approaches zero at T=0K, suggests that there is a component of the magnetic response that is following Curies law at the lowest temperatures, i.e. there is a non-interacting paramagnetic contribution. Note that the 5% Fe:TiO_2 annealed at T=800 ^{o} C shows a different magnetic character (see fig. 10d), and is indicative of the existence of a ferromagnetic component with T_C>350 K. A fit to the data is shown in figure 12 where it is assumed that an onset of ferromagnetic magnetic order can be described by a critical form and a Curie-Weiss function is used to describe the paramagnetic response observed at lower temperatures. In this case we obtain θ = 0K demonstrating that a non-interacting paramagnetic contribution dominates the low field/low temperature magnetic properties similar to the other samples investigated.

The origin of room temperature ferromagnetism (RTM) in TiO_2-based DMS is not clear and whether this behavior is an extrinsic i.e. caused by direct interaction between the local moments in magnetic impurity clusters or is an intrinsic due to exchange coupling between the spin of the carriers and the local magnetism is still debated.

In present work, we will not entirely rule out the possibility of the existence of ferromagnetic clusters or impurities in the doped TiO_2 lattice. However, the

observation of the RTFM in the undoped TiO_2 system can verify the role of defects in FM ordering in TiO_2 nanostructures [63, 64]. Santara et al. [56, 65] illustrated the role of large concentration of oxygen vacancies for the observed RTFM in doped and undoped TiO_2 nanoribbons.

From the literatures, the observed ferromagnetism in Fe-doped TiO_2 is attributed to the existence of several possible mechanisms such as double exchange and super exchange coupling [66], Ruderman-Kittel-Kasuya-Yoshida (RKKY) [67] and coupling of bound magnetic polarons (BMPs) [68], etc. While the dominant mechanism is still unclear, but it can be seen that the defects, carriers and/or their coupling play the vital role in all these models.

Chen et al. [66] predicted that oxygen vacancy enhances ferromagnetism in the Fe doped TiO_2 through a shallow impurity state of a nearest-neighbor Fe–oxygen vacancy complex or by the capture of vacancy electrons by the Fe atoms and consequent enhancement of the FM double exchange. Coey et al. [68] proposed the observed ferromagnetic behavior in terms of bound magnetic polaron (BMP). The BMP can be created by the influence of columbic interaction of paramagnetic oxygen vacancies with single electron (F^+ center) and the Fe^{3+} because of doping. In BMP model, the d-orbital of Fe^{3+} falls within the radius of F^+ center and consequently, the magnetic spins interact with the donor spins. All the dopant ions within the polaronic radius interact ferromagnetically and the overlap of several BMPs can create the long-range ferromagnetism.

The coupling between the two Fe^{3+} dopant spins through the oxygen vacancy with the trapped electron (F^+ center) leads to long-range FM ordering known as F-centre exchange coupling. When one of the Fe^{3+} is far away from the oxygen vacancy,

then antiferromagnetic interaction possibly occur by the existence of oxygen vacancies with two trapped electrons having $1s^2$ configuration [68].

Santara et al [56] pointed that the concentration of the dopant, the distribution of the dopant within the host lattice and energy level of the of the dopant can affect FM in Fe: TiO_2. The observed FM in Fe:TiO_2 samples were attributed most likely due to the exchange interaction between 3 d^5 spins of Fe^{3+} and the $1s^1$ spin of the F^+-centre

.

Therefore, it can be concluded that both oxygen vacancy and Fe dopant and their charge distribution within the TiO_2 lattice play an important role in increasing the FM ordering and enhancement of FM in Fe: TiO_2 nanostructures.

4. Conclusions

As a result, several features of magnetic properties of Fe: TiO_2 can be seen. At low doping level of 1% Fe, the magnetic ions are further apart from each other and are leading to a weaker interaction. The magnetic moment of free Fe^{3+} is evaluated about 5.9 μ_B, while the magnetic moment of the 1% Fe:TiO_2 annealed at T=400^o C is about 4.9 μ_B. Also the lower magnetization values for 5% Fe:TiO_2 annealed at T=400 ^{o} C and 1% Fe:TiO_2 annealed at T= 800^o C (3.2, and 2.9 μ_B) with respect to free Fe^{3+} ions is evaluated which reveals that spin correlations becomes prominent [22]. Observation of RTFM in the doped and undoped TiO_2 by Santara et al. [56] demonstrated the role of defects in FM ordering in TiO_2 nanostructures and shows that the oxygen vacancy mediates ferromagnetic (FM) interaction.

References:

[1] A.M. Tonejc, I. Djerdi, A. Tonejc, Evidence from HRTEM image processing, XRD and EDS on nanocrystalline iron-doped titanium oxide powders, Mat. Sci. Eng. B. 85 (2001) 55-63.
[2] Y. Zhang, Y. Shen, F. Gu, M. Wu, Y. Xie, J. Zhang, Influence of Fe ions in characteristics and optical properties of mesoporous titanium oxide thin films, Appl. Surf. Sci. 256 (2009) 85-89.
[3] Y. Matsumoto, M. Murakami, T. Shono, T. Hasegawa, T. Fukumura, M. Kawasaki, P. Ahmet, T. Chikyow, S.Y. Koshihara, H. Koinuma, Room-temperature ferromagnetism in transparent transition metal-doped titanium dioxide, Science 291 (2001) 854-856.
[4] S.A. Chambers, S. Thevuthasan, R.F.C. Farrow, R.F. Marks, J.U. Thiele, L. Folks, M.G. Samant, A.J. Kellock, N. Ruzycki, D.L. Ederer, U. Diebold, Epitaxial growth and properties of ferromagnetic co-doped TiO_2 anatase, Appl. Phys. Lett. 79 (2001) 3467-3469.
[5] A.F. Orlov, L.A. Balagurov, A.S. Konstantinova, N.S. Perov, D.G. Yarkin, Giant magnetic moments in dilute magnetic semiconductors, J. Magn. Magn. Mater. 320 (2008) 895-897.
[6] G. Talut, H. Reuther, J. Grenzer, S. Zhou, Origin of ferromagnetism in iron implanted rutile single crystals, Hyperfine Interact. 191 (2009) 95-102.
[7] C.Y. Wang, C. Bottcher, D.W. Bahnemann, J.K. Dohrmann, A comparative study of nanometer sized Fe(III)-doped TiO_2 photocatalysts: synthesis, characterization and activity, J. Mater. Chem. 13 (2003) 2322-2329.
[8] Y.H. Zhang, A. Reller, Nanocrystalline iron-doped mesoporous titania and its phase transition, J. Mater. Chem. 11 (2001) 2537-2541.
[9] M. Hirano, T. Joji, M. Inagaki, H. Iwata, Direct formation of iron (III)-doped titanium oxide (anatase) by thermal hydrolysis and its structure property, J. Am. Ceram. Soc. 87 (1) (2004) 35-41.
[10] N. Perkas, O. Palchik, I. Brukental, I. Nowik, Y. Gofer, Y. Koltypin, A. Gedanken, A mesoporous iron-titanium oxide composite prepared sonochemically, J. Phys. Chem. B. 107 (2003) 8772-8778.
[11] S.M. Oh, S.S. Kim, J.E. Lee, T. Ishigaki, D.W. Park, Effect of additives on photocatalytic activity of titanium dioxide powders synthesized by thermal plasma, Thin Solid Films 435 (2003) 252-258.
[12] A. Takeda, T. Sato, C. Kaito, S. Kaneko, Structure of metal doped TiO2 particles produced by RF plasma, Thin Solid Films 435 (2003) 211-214.
[13] R. Alexandrescu, I. Morjan, M. Scarisoreanu, R. Birjega, E. Popovici, I. Soare, L. Gavrila-Florescu, V.I. Sandu, F. Dumitrache, G. Prodan, E. Vasile, E. Figgemeier, Structural investigations on TiO_2 and Fe-doped TiO_2 nanoparticles synthesized by laser pyrolysis, Thin Solid Films 515 (2007) 8438-8445.
[14] X. Zhang, M. Zhou, L. Lei, Co-deposition of photocatalytic Fe doped TiO2 coatings by MOCVD, Catal. Commun. 7 (2006) 427-431.
[15] H. Yamashita, M. Harada, J. Misaka, M. Takeuchi, B. Neppolian, M. Anpo, Photocatalytic degradation of organic compounds diluted in water using visible light-responsive metal ion-implanted TiO_2 catalysts: Fe ion-implanted TiO_2, Catal. Today 84 (2003) 191-196.
[16] F. Gracia, J.P. Holgado, F. Yubero, A.R. Gonzalez-Felipe, Structural, optical, and photoelectrochemical properties of Mn^+-TiO_2 model thin film photocatalysts, J. Phys. Chem. B 108 (2004) 17466-17476.

[17] X.H. Wang, J.-G. Li, H. Kamiyama, M. Katada, N. Ohashi, Y. Moriyoshi, T. Ishigaki, Pyrogenic iron(III)-doped TiO_2 nanopowders synthesized in RF thermal plasma: phase formation, defect structure, band gap, and magnetic properties, J. Am. Chem. Soc. 127 (2005) 10982-10990.
[18] Y. Wang, H. Cheng, Y. Hao, J. Ma, W. Li, S. Cai, Preparation, characterization and photoelectrochemical behaviors of Fe(III)-doped TiO_2 nanoparticles, J. Mater. Sci. 34 (1999) 3721-3729.
[19] X.-Q. Chen, J.-Y. Yang, J.-S. Zhang, Preparation and photocatalytic properties of Fe-doped TiO_2 nanoparticles, J. Cent. South Univ. Technol. 11 (2004) 161-165.
[20] E.D. Jeong, P.H. Borse, J.S. Jang, J.S. Lee, O.-S. Jung, H. Chang, J.S. Jin, M.S. Won, H.G. Kim, Hydrothermal synthesis of Cr and Fe co-doped TiO2 nanoparticle photocatalyst, J. Ceram. Process. Res. 9 (2008) 250-253.
[21] F. Lin, D. Jiang, Y. Lin, X. Ma, Magnetism of Fe-doped TiO_2 milled in different milling atmospheres, Physica B 403 (2008) 2193-2196.
[22] C.E. Rodr´ıguez-Torres, A.F. Cabrera, L.A. Errico, C. Ad´an, F.G. Requejo, M. Weissmann, S.J. Stewart, Local structure and magnetic behaviour of Fe-doped TiO_2 anatase nanoparticles: experiments and calculations, J. Phys.: Condens. Matter 20 (2008) 1352101 -9.
[23] J. Ma, Y. Wei, W.-X. Liu, W.-B. Cao, Preparation of nanocrystalline Fe-doped TiO_2 powders as a visible-light-responsive photocatalyst, Res. Chem. Intermed. 35 (2009) 329-336.
[24] K. Melghit, O.S. Al-Shukeilia, I. Al-Amri, Effect of M-doping (M = Fe, V) on the photocatalytic activity of nanorod rutile TiO2 for Congo red degradation under the sunlight, Ceram. Int. 35 (2009) 433-439.
[25] M. Karimipour, J.M. Wikberg, V. Kapaklis, N. Shahtahmasebi, M. Rezaee Rokn Abad, M. Yeganeh, M.M. Bagheri-Mohagheghi, P. Svedlindh, Nanoparticles of Ni/NiO embedded in TiO2 synthesized by the complex-polymer sol–gel method , Phys. Scr. 84 (2011) 035702.
[26] M. Crisan, M. Raileanu, N. Dragan, D. Crisan, A. Ianculescu, I. Nitoi, P. Oancea, S. Somacescu, N. Stanica, B. Vasile, C. Stan, Sol-gel iron-doped TiO_2 nanopowders with photocatalytic activity, Appl. Catal. A. 504 (2015) 130-142.
[27] K. Oganisian, A. Hreniak, A. Sikora, D. Gaworska-Koniarek, A. Iwan, Synthesis of iron doped titanium dioxide by sol-gel method for magnetic applications, Process. Appl. Ceram. 1 (2015) 43-51.
[28] N. Shimizu, K. Yamaki, T. Mochiku, V. Yamada, S. Itoh, K. Kadowaki, Ferromagnetism in diluted magnetic semiconductors $Ti_{1-x}M_xO_2$ (M = V, Cr, Mn and Ni), Phys. Stat. Sol. (c) 3 (2006) 4151-4154.
[29] E.A. Kozlova, T.P. Korobkina, A.V. Vorontsov, V.N. Parmon, Enhancement of the O_2 or H_2 photoproduction rate in a Ce^{3+}/Ce^{4+}-TiO_2 system by the TiO_2 surface and structure modification, Appl. Catal. A. 367 (2009) 130-137.
[30] C.K. Chan, J.F. Porter, Y.G. Li, W. Guo, C.M. Chan, Effects of calcination on the microstructures and photocatalytic properties of nanosized titanium dioxide powders prepared by vapor hydrolysis, J. Am. Ceram. Soc. 82 (1999) 566-572.
[31] L. Gao, Q.H. Zhang, Effects of amorphous contents and particle size on the photocatalytic properties of TiO_2 nanoparticles, Scripta Materialia 44 (2001) 1195-1198.
[32] N.L. Wu, M.S. Lee, Z.J. Pon, J.Z. Hsu, Effect of calcination atmosphere on TiO_2 photocatalysis in hydrogen production from methanol/water solution, J. Photochem. Photobiol. A 163 (2004) 277-280.

[33] G.K. Wiliamson, W.H. Hall, X-ray line broadening from filed aluminium and wolfram, Acta. Metall. 1 (1953) 22-31.
[34] V. Biju, N. Sugathan, V. Vrinda, S.L. Salini, Estimation of lattice strain in nanocrystalline silver from X-ray diffraction line broadening, J. Mater. Sci. 43 (2008) 1175-1179.
[35] M.B. Kerber, E. Schafler, M. Zehetbauer, Processing and evaluation of X-ray line profiles measured from nanostructured materials produced by sever plastic deformation, Rev. Adv. Mater. Sci. 10 (2005) 427-433.
[36] B. Choudhury, A. Choudhury, Local structure modification and phase transformation of TiO2 nanoparticles initiated by oxygen defects, grain size, and annealing temperature, Int. Nano Lett. (2013) 1-9.
[37] A. Maurya, P. Chauhan, S.K. Mishra, R.K. Srivastava, Structural, optical and charge transport study of rutile TiO2 nanocrystals at two calcination temperatures, J. Alloys. Compd. (2011) 8433-8440.
[38] K.M. Prabu, S. Perumal, Micro strain and Morphological studies of anatase and rutile TiO2 nanocrystals prepared via sol-gel and solvothermal method - A comparative study, Int. J. Sci. Res. Sci. Eng. Technol. 1/4 (2015) 299-304.
[39] H. Milani Moghaddam, S. Nasirian, Dependence of activation energy and lattice strain on TiO2 nanoparticles?, Nanosci. Method 1 (2016) 201-212.
[40] U. Diebold, The surface science of titanium dioxide, Surf. Sci. Rep. 48 (2003) 53-229.
[41] B. Choudhury, R. Verma, A. Choudhury, Oxygen defect assisted paramagnetic to ferromagnetic conversion in Fe doped TiO_2 nanoparticles, RSC Adv. 4 (2014) 29314-29323.
[42] H. Zhang, J.F. Banfield, Thermodynamic analysis of phase stability of nanocrystalline titania, J. Mater. Chem. 8 (1998) 2073-2076.
[43] A.A. Gribb, J.F. Banfield, Particle size effects on transformation kinetics and phase stability in nanocrystalline TiO_2, Am. Mineral. 82 (1997) 717-728.
[44] H. Zhang, J.F. Banfield, Understanding polymorphic phase transformation behavior during growth of nanocrystalline aggregates: insights from TiO_2, J. Phys. Chem. B 104 (2000) 3481-3487.
[45] W. Li, C. Ni, H. Lin, C.P. Huang, S.I. Shah, Size dependence of thermal stability of TiO_2 nanoparticles, J. Appl. Phys. 96 (2004) 6663-6668.
[46] M. Okada, P. Jing, Y. Yamada, M. Tazawa, K. Yoshimura, Low-energy electron energy loss spectroscopy of rutile and anatase TiO_2 films in the core electron excitation regions, Surf. Sci. 566 (2004) 1030-1034.
[47] E. Stoyanov, F. Langenhorst, G. Steinle-Neumann, The effect of valence state and site geometry on Ti $L_{3,2}$ and O K electron energy-loss spectra of Ti_xO_y phases, Am. Mineral. 92 (2007) 577-586.
[48] D.W. Fischer, Molecular-Orbital interpretation of the soft X-ray $L_{3,2}$ emission and absorption spectra from some titanium and vanadium compounds, J. Appl. Phys. 41 (1970) 3561-3569.
[49] R.D. Leapman, L.A. Grunes, P.L. Fejes, Study of the $L_{2,3}$ edges in the 3d transition metals and their oxides by electron-energy-loss spectroscopy with comparisons to theory, Phys. Rev. B. 26 (1982) 614-635.
[50] F.M.F. de Groot, X-ray absorption and dichroism of transition metals and their compounds, J. Electron Spectrosc. Relat. Phenom. 61 (1994) 529-622.
[51] N.D. Abazovic, L. Mirenghi, I.A. Jankovic, N. Bibic, D.V. Šojic, B.F. Abramovic, M. Comor, Synthesis and characterization of rutile TiO_2 nanopowders doped with iron ions, Nanoscale Res. Lett. 4 (2009) 518-525.

[52] Y. Wu, J. Zhang, L. Xiao, F. Chen, Properties of carbon and iron modified TiO_2 photocatalyst synthesized at low temperature and photodegradation of acid orange 7 under visible light, Appl. Surf. Sci. 256 (2010) 4260-4268.
[53] J. Yu, Q. Xiang, M. Zhou, Preparation, characterization and visible-light-driven photocatalytic activity of Fe-doped titania nonorods and first-principles study of electronic structures, Appl. Catal. B: Environ. 90 (2009) 595-602.
[54] J. Zhang, X. Chen, Y. Shen, Y. Li, Z. Hu, J. Chu, Synthesis, surface morphology, and photoluminescence properties of anatase iron-doped titanium dioxide nano-crystalline films, Phys. Chem. Chem. Phys. 13 (2011) 13096-13105.
[55] N. Nasralla, M. Yeganeh, Y. Astuti, S. Piticharoenphun, N. Shahtahmasebi, A. Kompany, M. Karimipour, B.G. Mendis, N.R.J. Poolton, L. Šiller, Structural and spectroscopic study of Fe-doped TiO_2 nanoparticles prepared by sol–gel method, Scientia Iranica F 20 (2013) 1018-1022.
[56] B. Santara, P.K. Giri, S. Dhara, K. Imakita, M. Fujii, Oxygen vacancy-mediated enhanced ferromagnetism in undoped and Fe-doped TiO_2 nanoribbons, J. Phys. D: Appl. Phys. 47 (2014) 235304 (14 pp).
[57] B. Leedahl, D.A. Zatsepin, D.W. Boukhvalov, R.J. Green, J.A. McLeod, S.S. Kim, E.Z. Kurmaev, I.S. Zhidkov, N.V. Gavrilov, S.O. Cholakh, A. Moewes, Structural defects induced by Fe-ion implantation in TiO_2, J. App. Phys. 115 (2014) 053711 (7 pp).
[58] H.W. Nesbitt, I.J. Muir, X-ray photoelectron spectroscopic study of a pristine pyrite surface reacted with water vapour and air, Geochim. Cosmochim. Acta. 58 (1994) 4667-4679.
[59] T. Droubay, S.A. Chambers, urface-sensitive Fe 2p photoemission spectra for α-Fe_2O_3(0001): The influence of symmetry and crystal-field strength, Phys. Rev. B. 64 (2001) 205414.
[60] S. Hüfner, photoelectron spectroscopy. Principles and applications, third ed., Springer, Berlin Heidelberg, 2003.
[61] N. Akdogan, A. Nefedov, A. Westphalen, H. Zabel, R.I. Khaibullin, L.R. Tagirov, Dose dependence of magnetism in Co-doped TiO_2, Superlatt. Microstr. 41 (2007) 132-137.
[62] D.H. Kim, J.S. Yang, Y.S. Kim, D.-W. Kim, T.W. Noh, S.D. Bu, Y.-W. Kim, Y.D. Park, S.J. Pearton, Y. Jo, J.-G. Park, Superparamagnetism in Co-ion-implanted anatase TiO2 thin films and effects of postannealing, Appl. Phys. Lett. 83 (2003) 4574-4576.
[63] N. Hoa, D. Huyen, Comparative study of room temperature ferromagnetism in undoped and Ni-doped TiO_2 nanowires synthesized by solvothermal method, J. Mater. Sci.: Mater. Electron. 24 (2013) 793-798.
[64] N.H. Hong, J. Sakai, N. Poirot, V. Briz´e, Room-temperature ferromagnetism observed in undoped semiconducting and insulating oxide thin films, Phys. Rev. B. 73 (2006) 132404.
[65] B. Santara, P.K. Giri, K. Imakita, M. Fujii, Evidence of oxygen vacancy induced room temperature ferromagnetism in solvothermally synthesized undoped TiO_2 nanoribbons, Nanoscale 5 (2013) 5476-5488.
[66] J. Chen, P. Rulis, L. Ouyang, S. Satpathy, W.Y. Ching, Vacancy-enhanced ferromagnetism in Fe-doped rutile TiO_2, Phys. Rev. B 74 (2006) 235207.
[67] Z. Wang, W. Wang, J. Tang, L.D. Tung, L. Spinu, W. Zhou, Extraordinary Hall effect and ferromagnetism in Fe-doped reduced rutile, Appl. Phys. Lett. 83 (2003) 518-520.

[68] J.M.D. Coey, M. Venkatesan, C.B. Fitzgerald, Donor impurity band exchange in dilute ferromagnetic oxides, Nat. Mater. 4 (2005) 173-179.

Captions:

Table1: The XRD parameters and mean size of particles in different crystallography orientations at different annealing temperatures

Table 2: The Ti $L_{3,2}$ lines and O K-edge peak position observed in EELS spectrum and also from ref [47].

Table 3: Binding energy (eV) for Ti $2p_{3/2}$ (with its spin-orbit splitting value) in 1%, and 5% Fe doped TiO_2 calcined at 400 ^oC, 600 ^oC, and 800 ^oC.

Table 4: The coercivity field and the remanence magnetization of the samples

Figure 1: The XRD patterns of the prepared samples.

Figure 2: HRTEM and electron diffraction patterns of 1% Fe doped TiO_2 annealed at (a) 400^{o}C, (b) 600^{o}C and (c) 800^{o}C.

Figure 3: HRTEM images of 5% Fe doped in TiO_2 annealed at (a) 400^{o}C, (b) 600^{o}C and (c) 800^{o}C.

Figure 4: EELS spectrum of 1% and 5% Fe doped TiO_2 annealed at 400^{o}C and 600^{o}C.

Figure 5: High resolution XPS core level and fittings of Fe 2p spectrum of the (a) 1% and (b) 5% Fe annealed at 800 ^{o}C and

Figure 6: High resolution XPS core level Ti 2p spectrum of 5%Fe doped TiO_2 calcined at 400^o, 600^o, and 800 ^{o}C.

Figure 7: Hysteresis loop of the (A) 1% and (B) 5% Fe doped TiO_2 annealed at 400^{o}C and 800^{o}C .(C) and (D) M-H curves of the samples at 5 K . (Scatters show the experimental results and solid lines are the result of fitting as described in the text)

Figure 8: Magnetization of 5% Fe doped TiO_2 annealed at 800^{o}C at room temperature.

Figure 9: Comparison of the magnetization measured at 5 and 300K against H/T for 5%Fe:TiO_2 annealed at 800^oC. The inset of the figure shows the enlargement of hysteresis loops of this sample measured at 300K near the origin.

Figure 10: FC and ZFC magnetization curves of Fe dope TiO_2

Figure 11: $(M/H)^{-1}$curves of the samples and the linear fits.

Figure 12: Magnetization of 5% Fe doped TiO_2 annealed at 800^oC against temperature (hollow circles) and the fitted curve (solid line)

Table 1

Dopant ratio (Fe/Ti)%	Annealing Temperature (^{o} C)	Crystalline structure	Phase composition (%)	a	b	c	Particle mean size (nm) By W-H plot	Lattice strain
1	400	Anatase	72.27	3.77600	3.77600	9.48600	11	0.00131441
		Rutile	27.73	4.59330	4.59330	2.95920		
1	600	Anatase	16.84	3.78300	3.78300	9.510	26	0.00076157
		Rutile	83.16	4.59330	4.59330	2.95920		
1	800	Rutile	100	4.59330	4.59330	2.95920	33	-0.00005141
5	400	Anatase	68.15	3.78520	3.78520	9.513	10	0.00086452
		Rutile	31.9	4.58000	4.58000	2.95000		
5	600	Anatase	11.45	3.78520	3.78520	9.513	23	-0.00068493
		Rutile	88.55	4.59330	4.59330	2.95920		
5	800	Rutile	100	4.59330	4.59330	2.95920	41	0.0007001

Table 2

Sample	Ti $L_{2,3}$ edge peak position (eV)				O K-edge peak position (eV)				
	L_3		L_2						
	a	b	c	d	A	B	C	D	E
TiO_2 rutile [47]	458.3	460.0	~464	~466.3	531.1	533.7	~540.0	542.9	~545.6
TiO_2 anatase [47]	458.3	460.0	~464	~466.3	531.0	533.5	539.6	543.9	~545.3

	Ti $L_{2,3}$ edge peak position		O K-edge peak position			Fe L_3 edge peak position
	L_3	L_2				
1%Fe:TiO_2 T=400^{o}C	458	463	531	541		
5%Fe:TiO_2 T=600^{o}C	461	466	531	534	543	708

Table 3

Iron concentration	Binding Energy (peak separation) (eV)		
	At 400^{o}C	At 600^{o}C	At 800^{o}C
1% Fe	458.7 (5.7)	458.5 (5.7)	458.1 (5.7)
5% Fe	458.4 (5.7)	458.4 (5.8)	458.3 (5.8)

Table 4

Impurity concentration	Annealed Temperature (^oC)	T(K)	Coercivity field (O e)	Remanence magnetization (emu/g)
Fe 1%	400	5	14	0.001
Fe 5%	800	5	200	0.005
Fe 5%	800	RT	370	0.0006

Figure 1

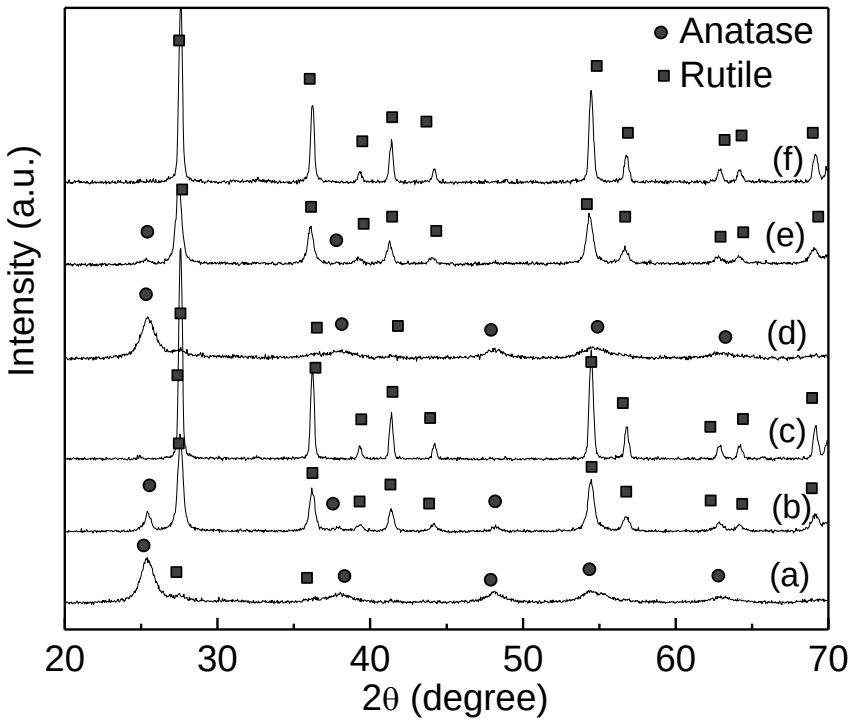
Anatase
Rutile
(f)
(e)
(d)
(c)
(b)
(a)
Intensity (a.u.)
20
30
40
50
60
70
2θ (degree)

Figure2

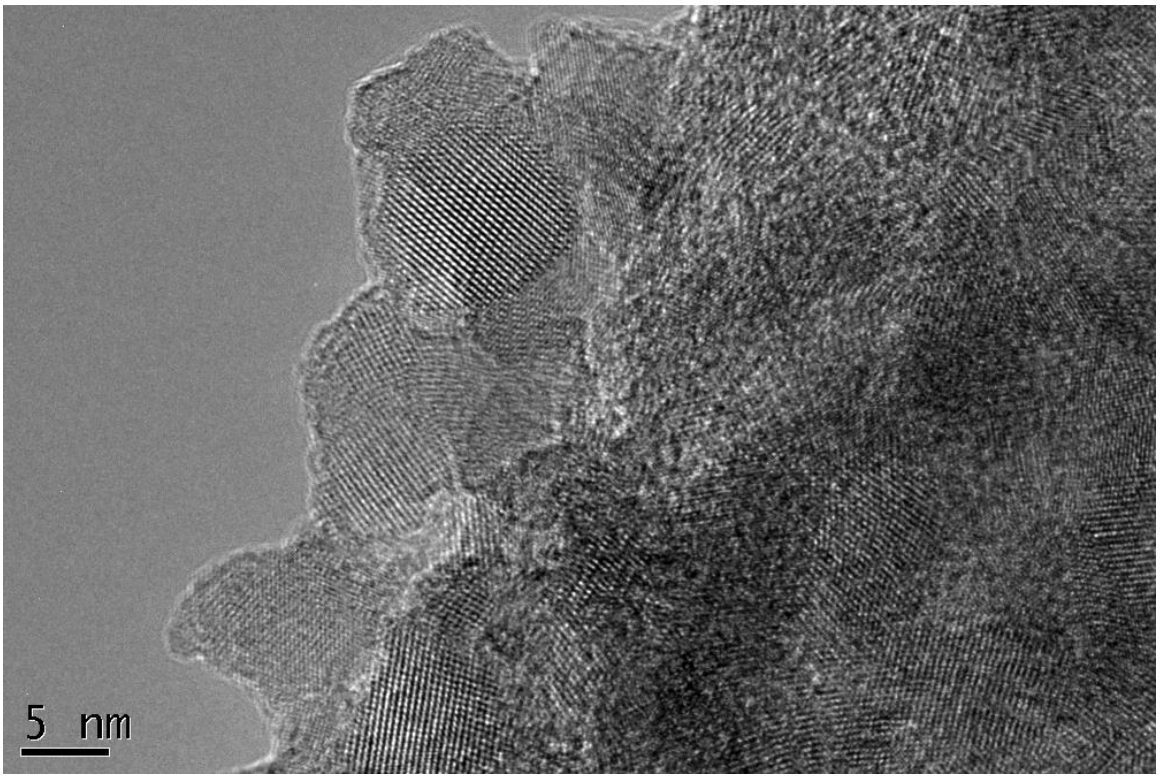

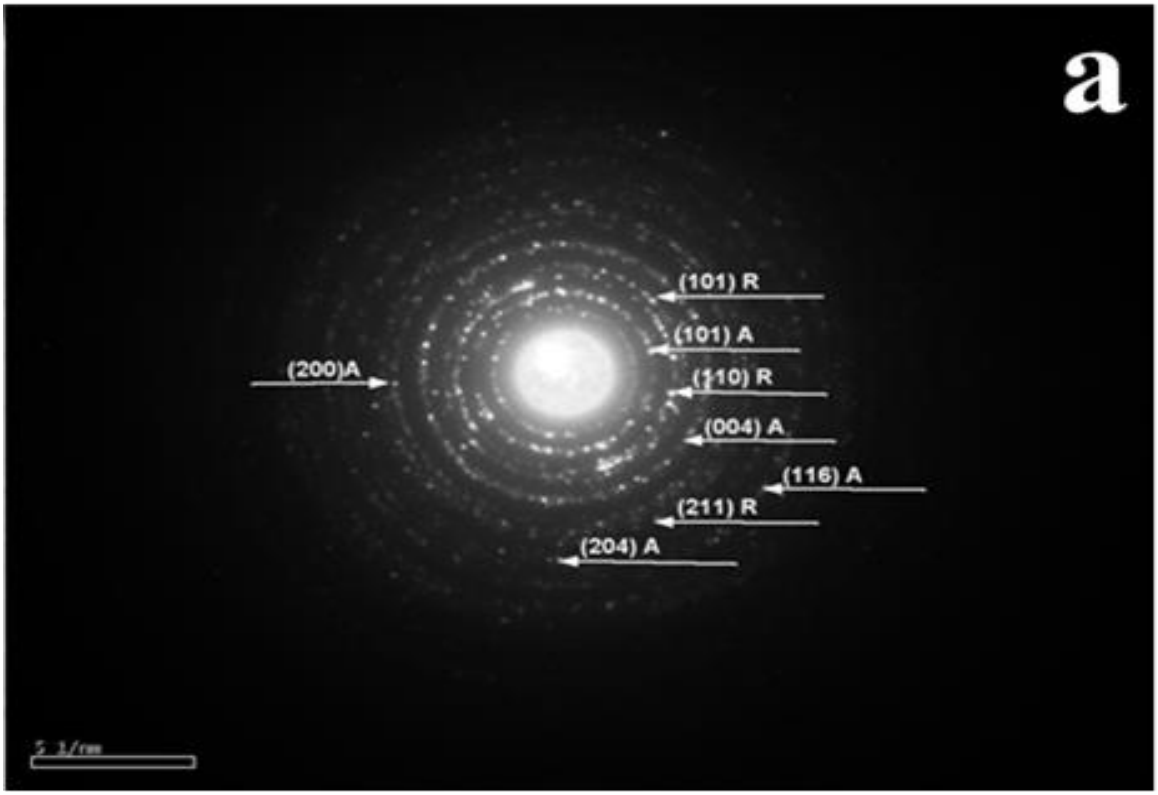

(a)

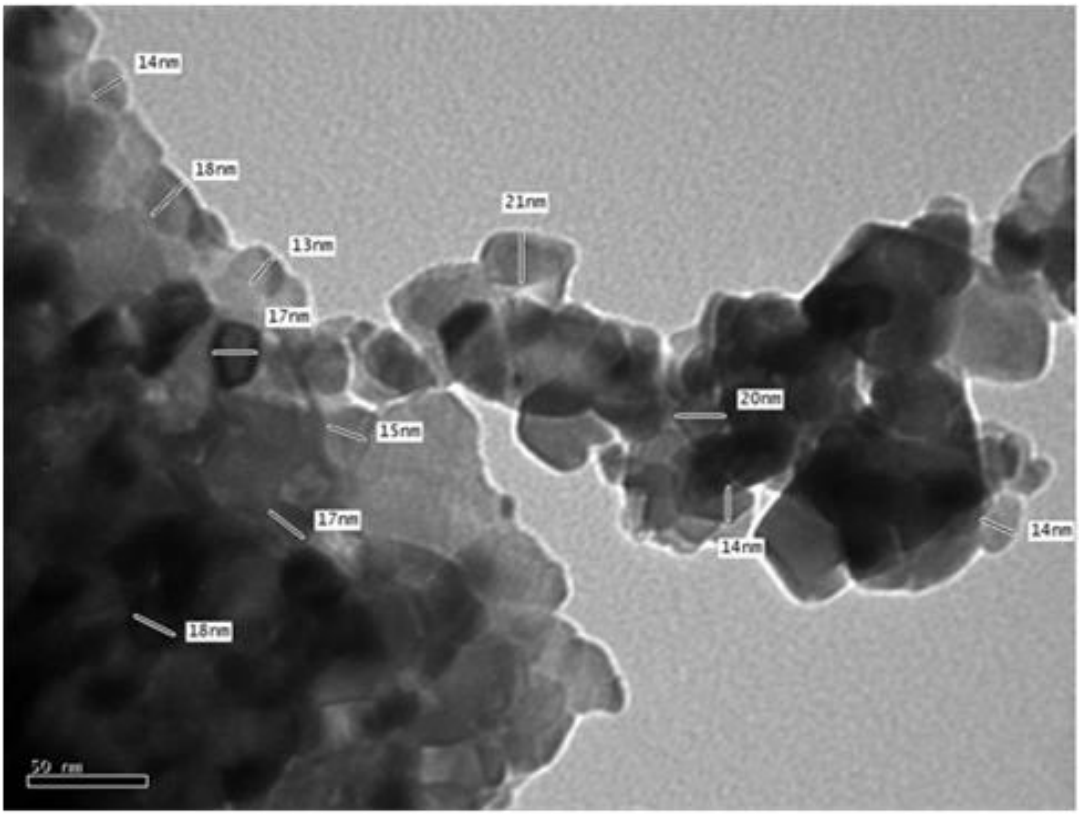
14nm
18nm
21nm
13nm
17nm
20nm
15nm
17nm
14nm
14nm
18nm
50 nm

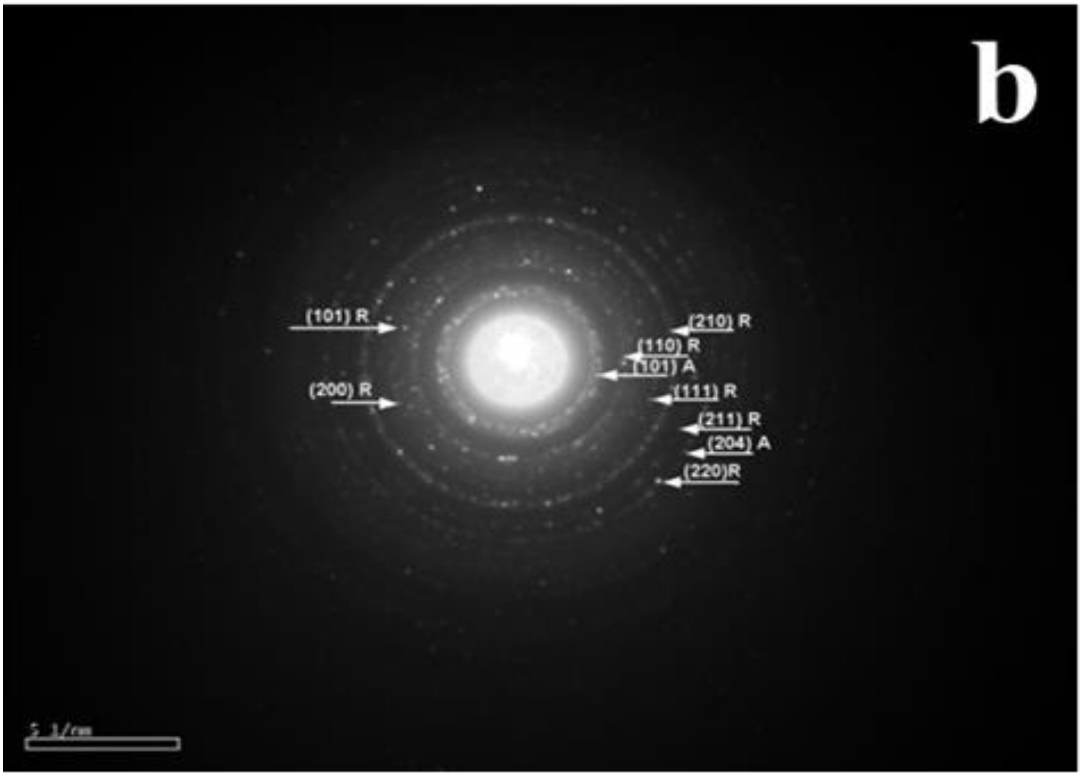
b
(101) R
(210) R
(110) R
(101) A
(200) R
(111) R
(211) R
(204) A
(220)R
5 1/nm

(b)

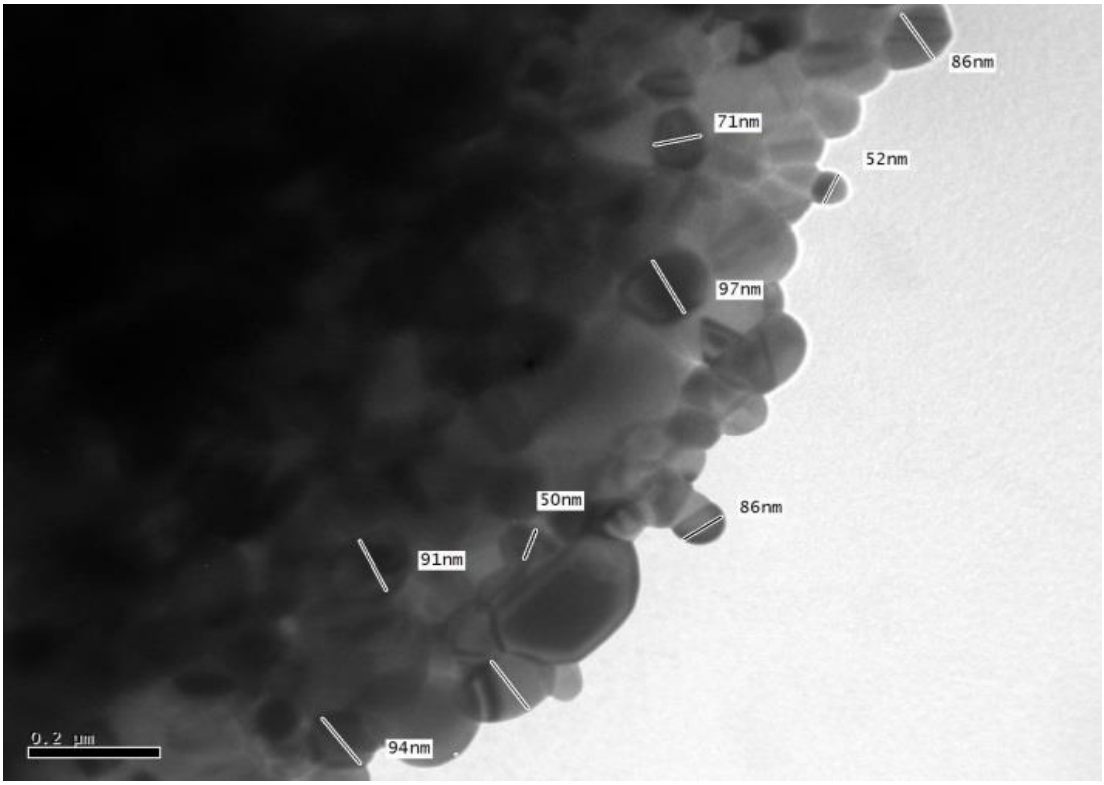
86nm
71nm
52nm
97nm
50nm
86nm
91nm
94nm
0.2 µm

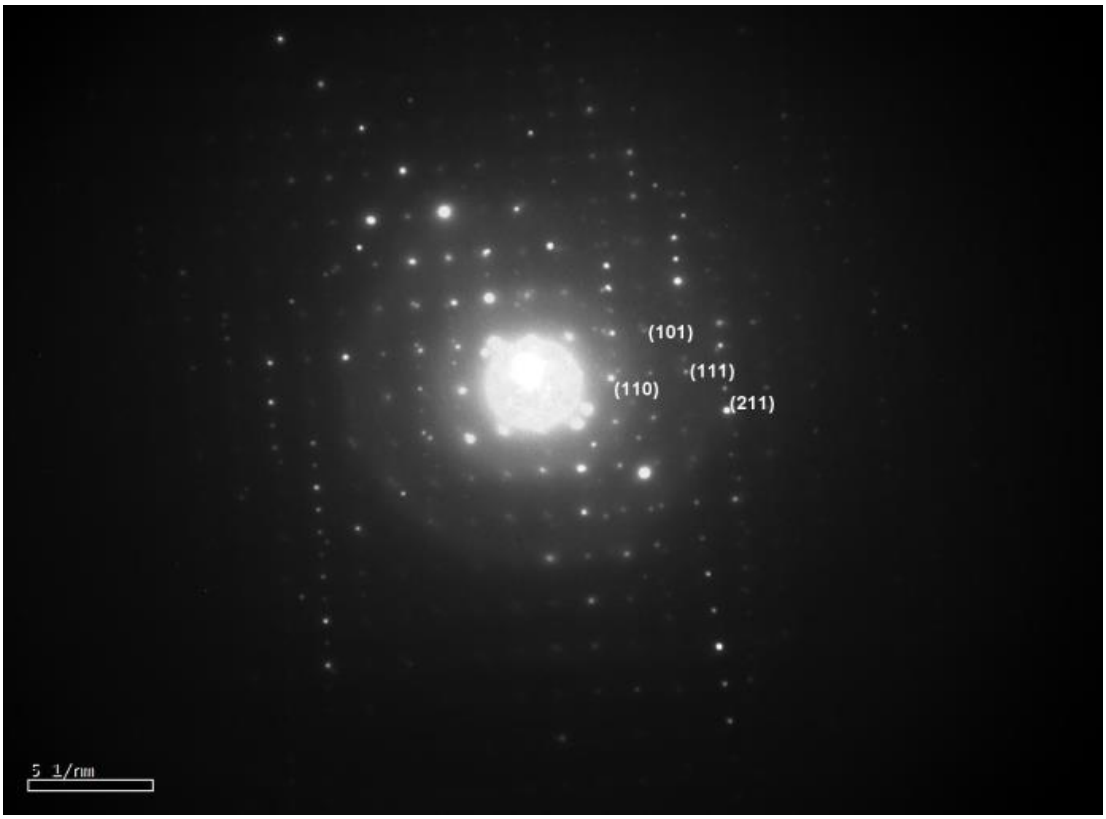
(101)
(111)
(110)
(211)
5 1/nm

(c)

Figure 3

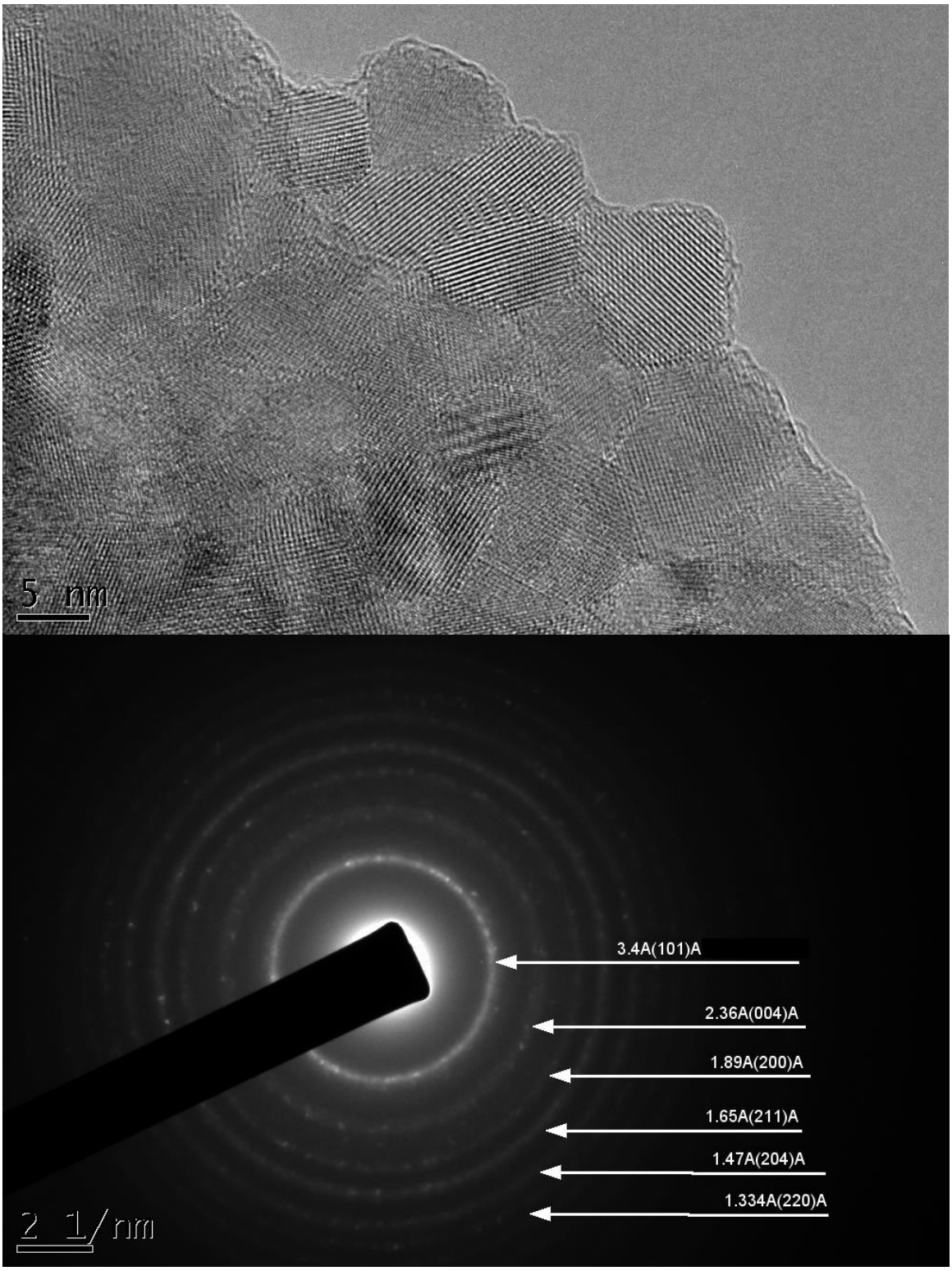
5 nm
3.4A(101)A
2.36A(004)A
1.89A(200)A
1.65A(211)A
1.47A(204)A
1.334A(220)A
2 1/nm

(a)

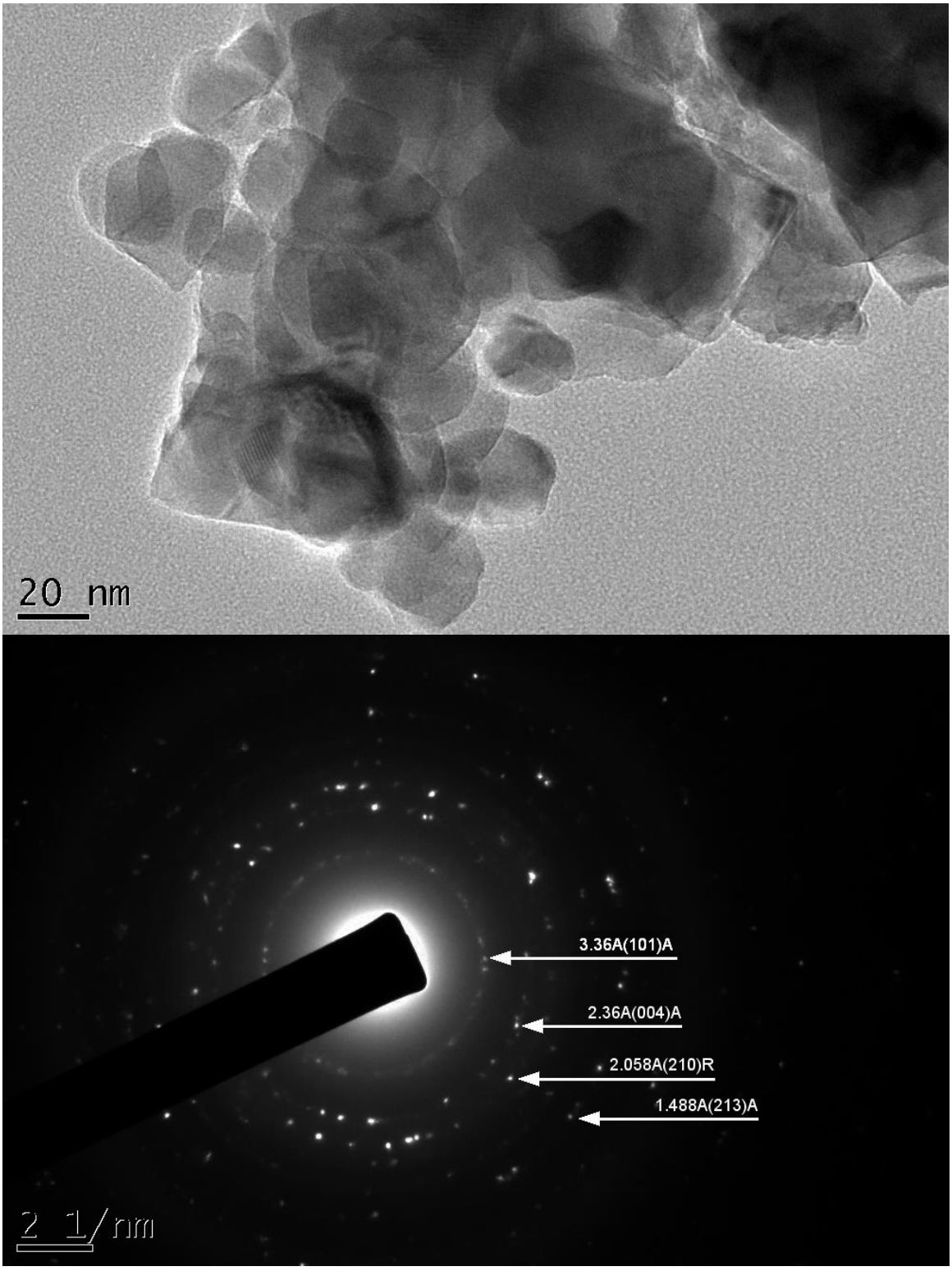

(b)

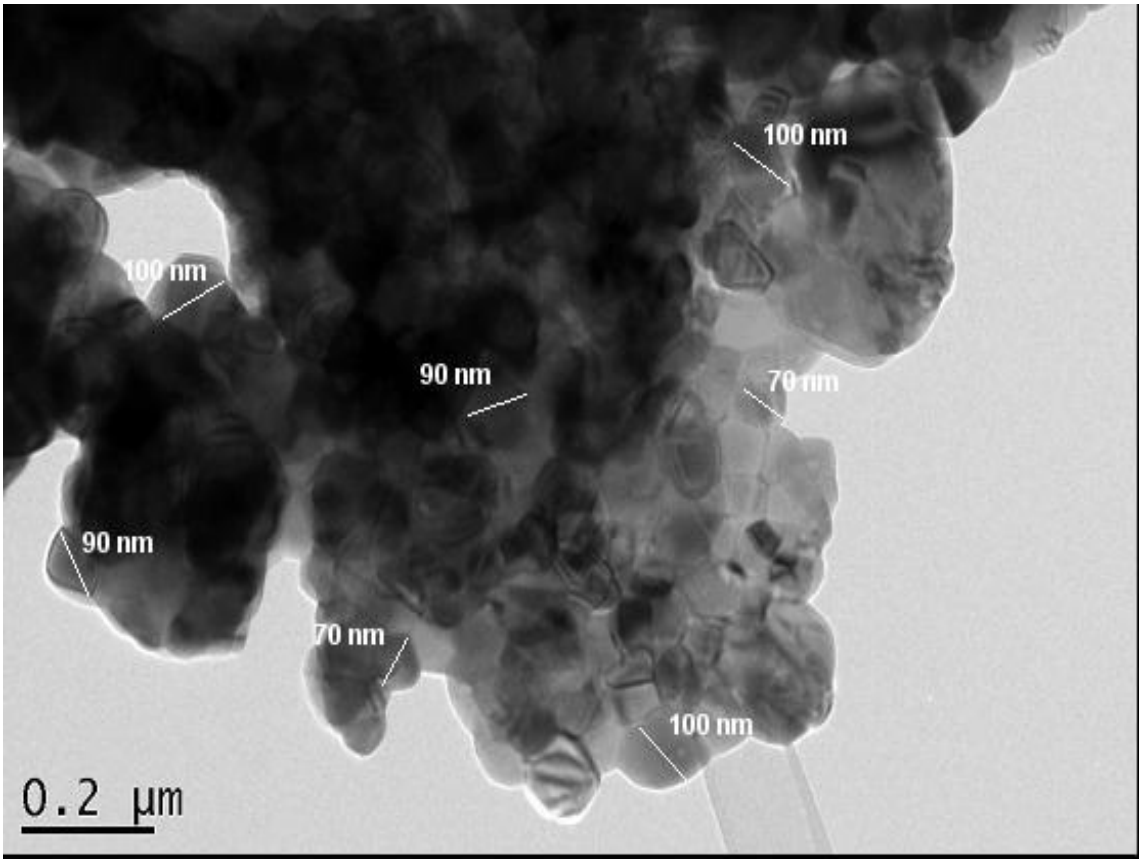
100 nm
100 nm
90 nm
70 nm
90 nm
70 nm
100 nm
0.2 µm

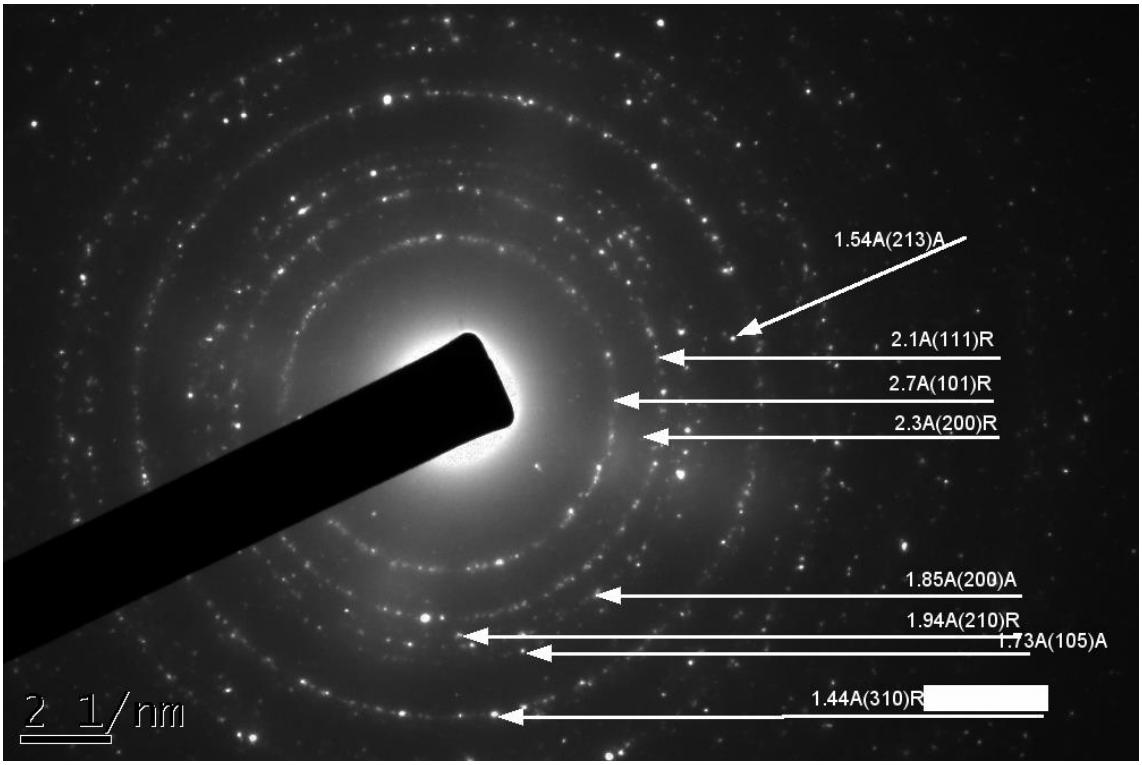
1.54A(213)A
2.1A(111)R
2.7A(101)R
2.3A(200)R
1.85A(200)A
1.94A(210)R
1.73A(105)A
1.44A(310)R
2 1/nm

(c)

Figure 4

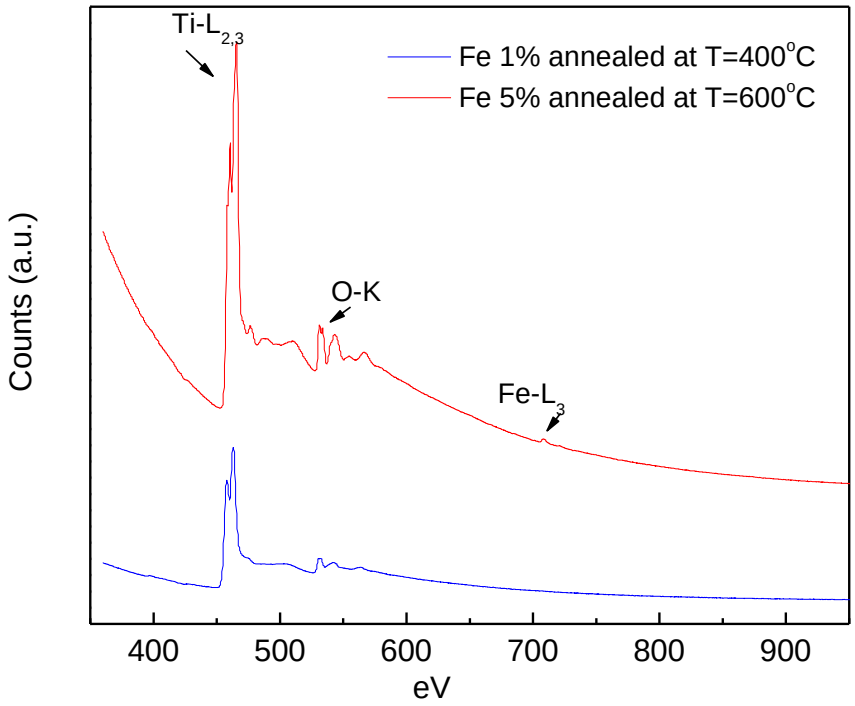
Ti-L2,3
Fe 1% annealed at T=400°C
Fe 5% annealed at T=600°C
O-K
Fe-L3
Counts (a.u.)
400
500
600
700
800
900
eV

Figure 5:

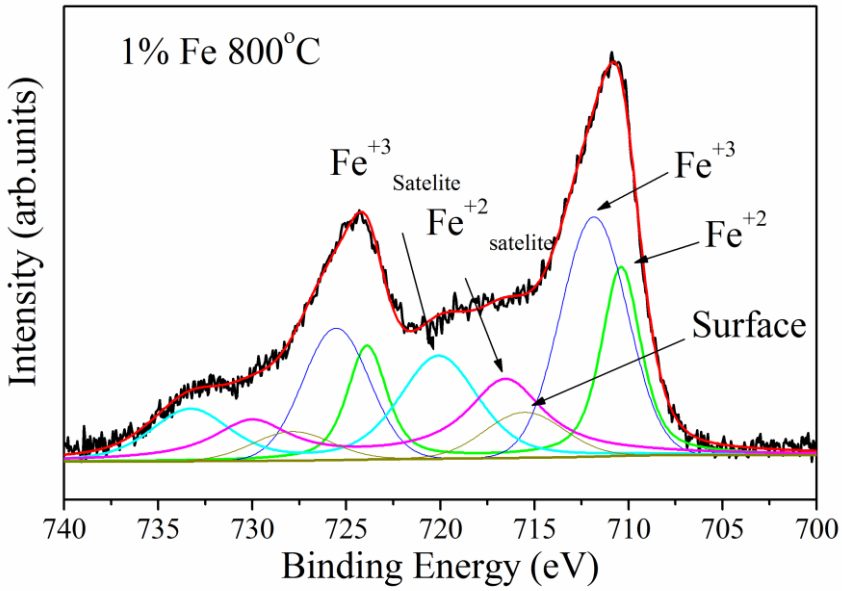
1% Fe 800°C
Intensity (arb.units)
Fe+3 Satelite
Fe+2 satelite
Fe+3
Fe+2
Surface
740 735 730 725 720 715 710 705 700
Binding Energy (eV)

(a)

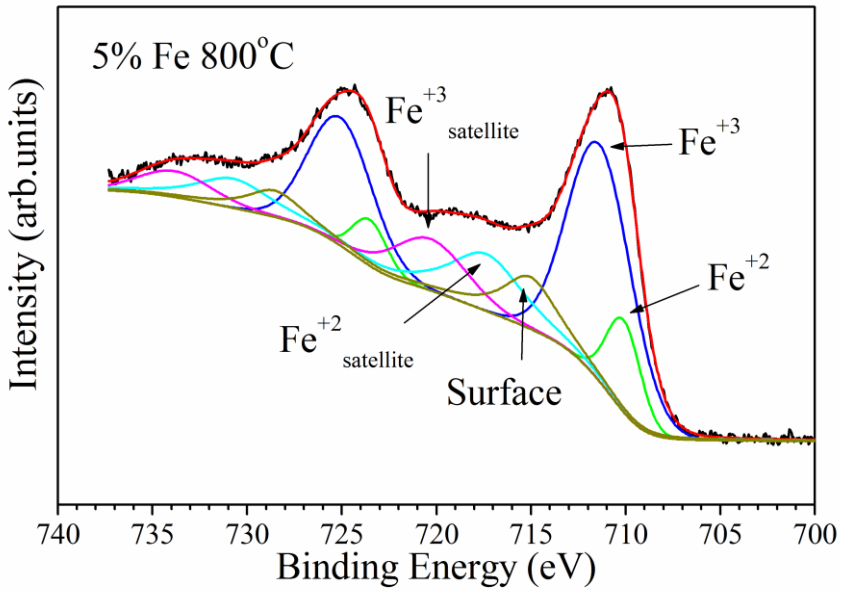
5% Fe 800°C
Intensity (arb.units)
Fe+3 satellite
Fe+3
Fe+2
Fe+2 satellite
Surface
740 735 730 725 720 715 710 705 700
Binding Energy (eV)

(b)

Figure 6:

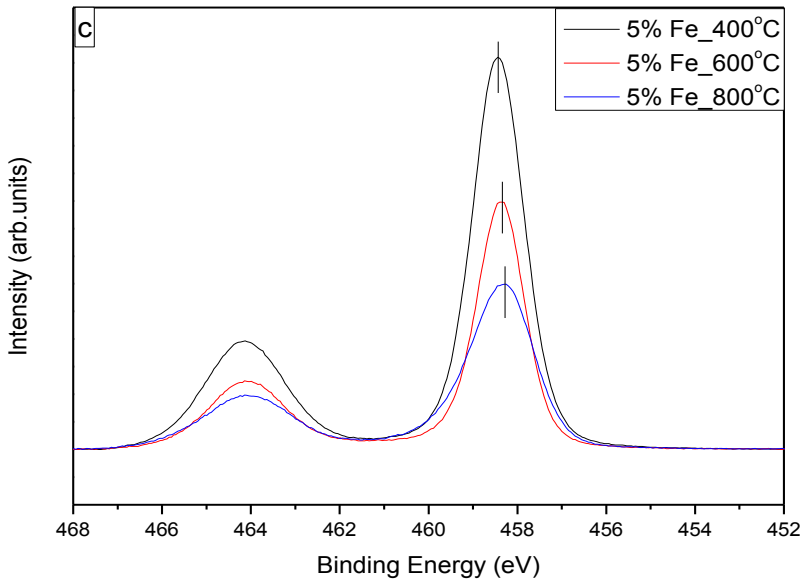
C
5% Fe_400°C
5% Fe_600°C
5% Fe_800°C
Intensity (arb.units)
468
466
464
462
460
458
456
454
452
Binding Energy (eV)

Figure 7

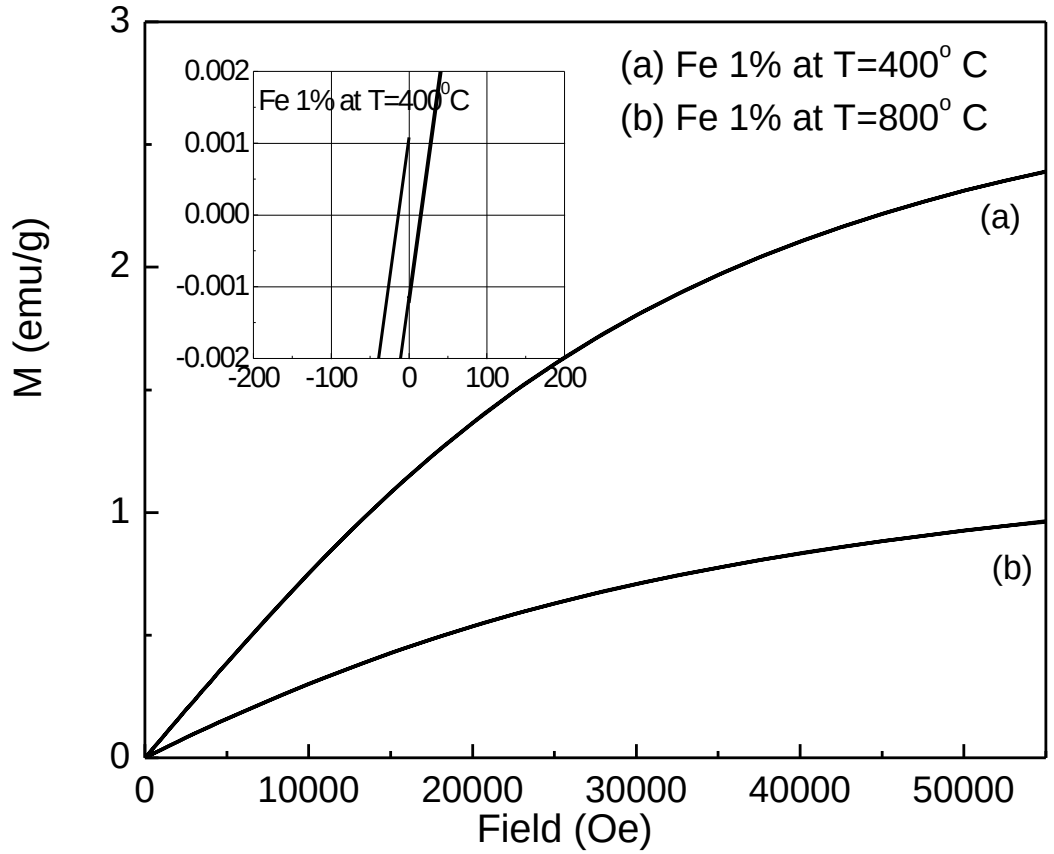
(a) Fe 1% at T=400° C
(b) Fe 1% at T=800° C
Fe 1% at T=400° C
M (emu/g)
Field (Oe)
(a)
(b)
0.002
0.001
0.000
-0.001
-0.002
-200
-100
0
100
200
0
1
2
3
10000
20000
30000
40000
50000

(A)

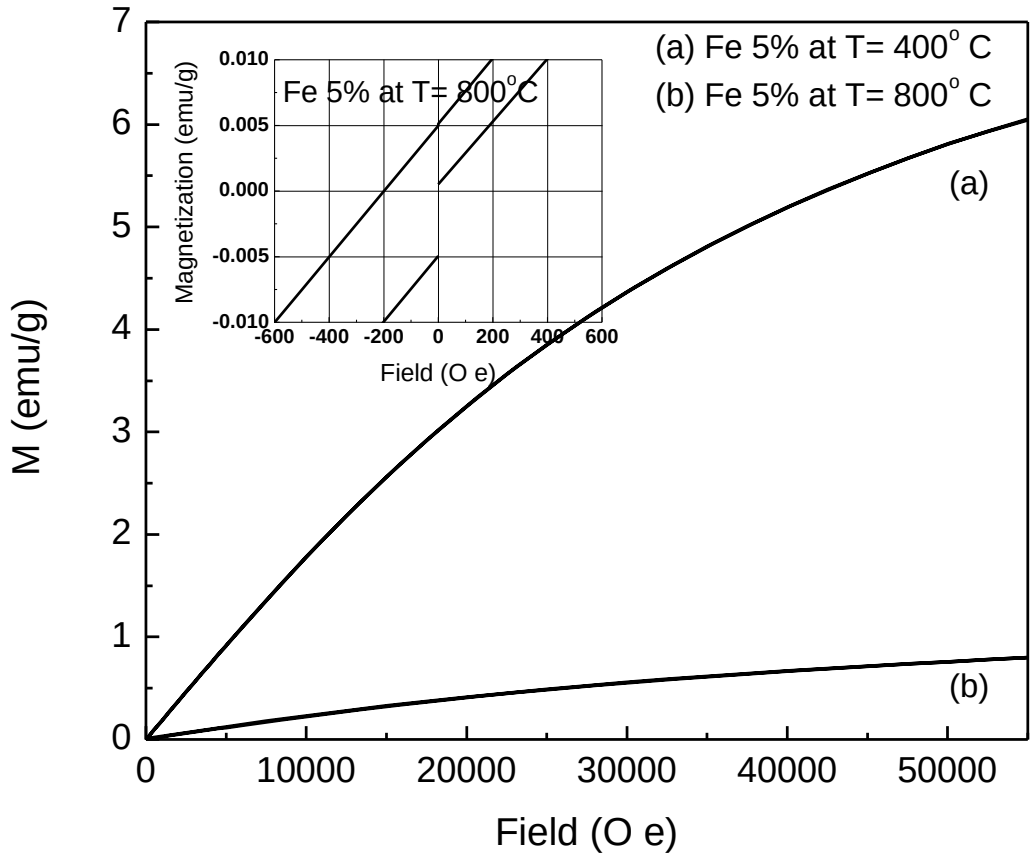
(a) Fe 5% at T= 400° C
(b) Fe 5% at T= 800° C
Fe 5% at T= 800° C
Magnetization (emu/g)
Field (O e)
M (emu/g)
Field (O e)
(a)
(b)

(B)

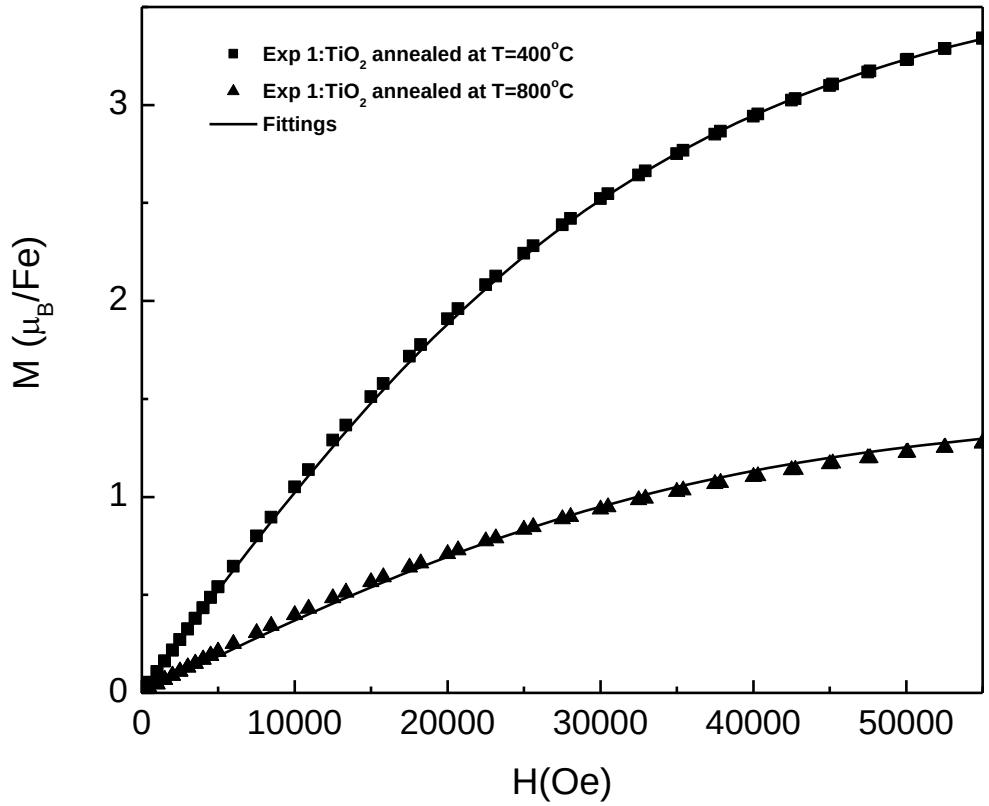
Exp 1:TiO2 annealed at T=400°C
Exp 1:TiO2 annealed at T=800°C
Fittings
M (μB/Fe)
H(Oe)
0
1
2
3
0
10000
20000
30000
40000
50000

(C)

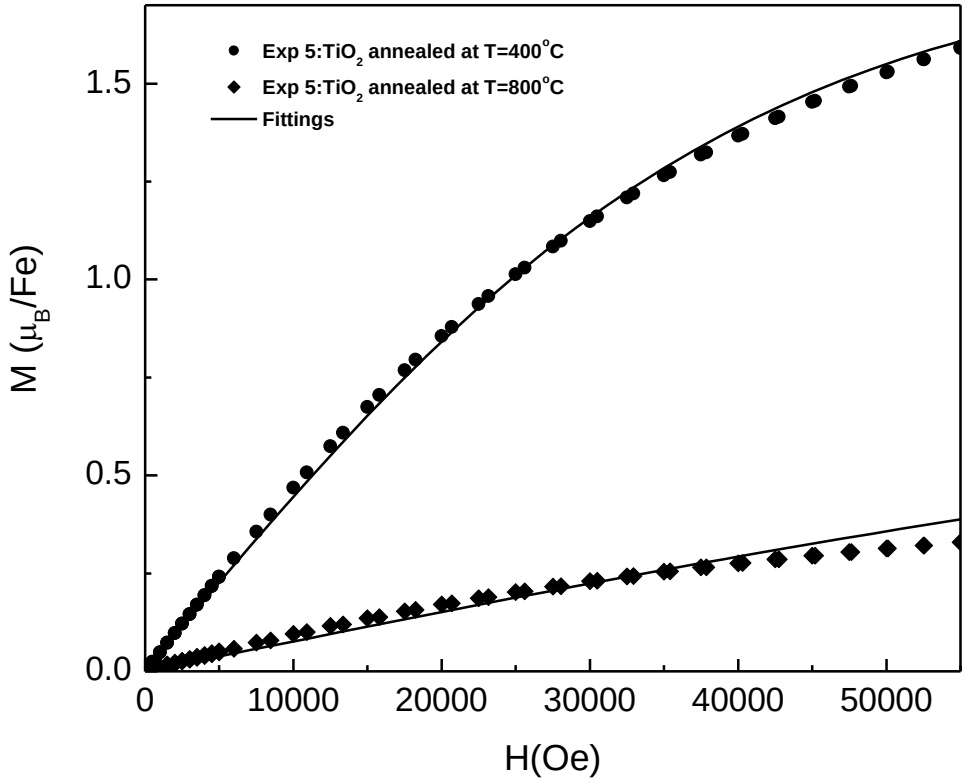
Exp 5:TiO2 annealed at T=400°C
Exp 5:TiO2 annealed at T=800°C
Fittings
M (μB/Fe)
H(Oe)
0.0
0.5
1.0
1.5
0
10000
20000
30000
40000
50000

(D)

Figure 8

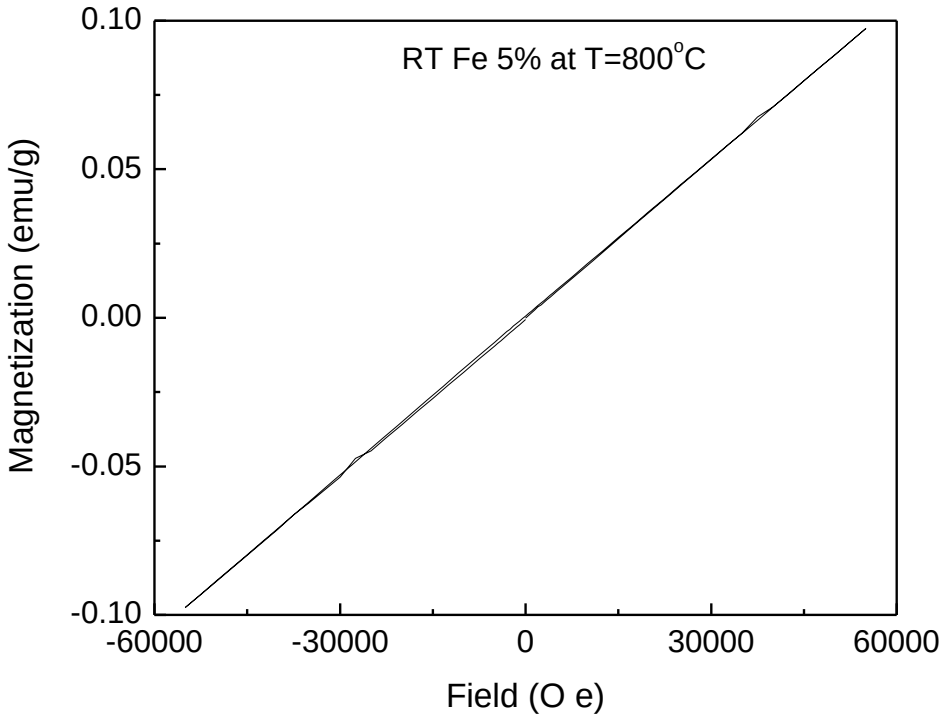
RT Fe 5% at T=800°C
Magnetization (emu/g)
0.10
0.05
0.00
-0.05
-0.10
-60000
-30000
0
30000
60000
Field (O e)

Figure 9

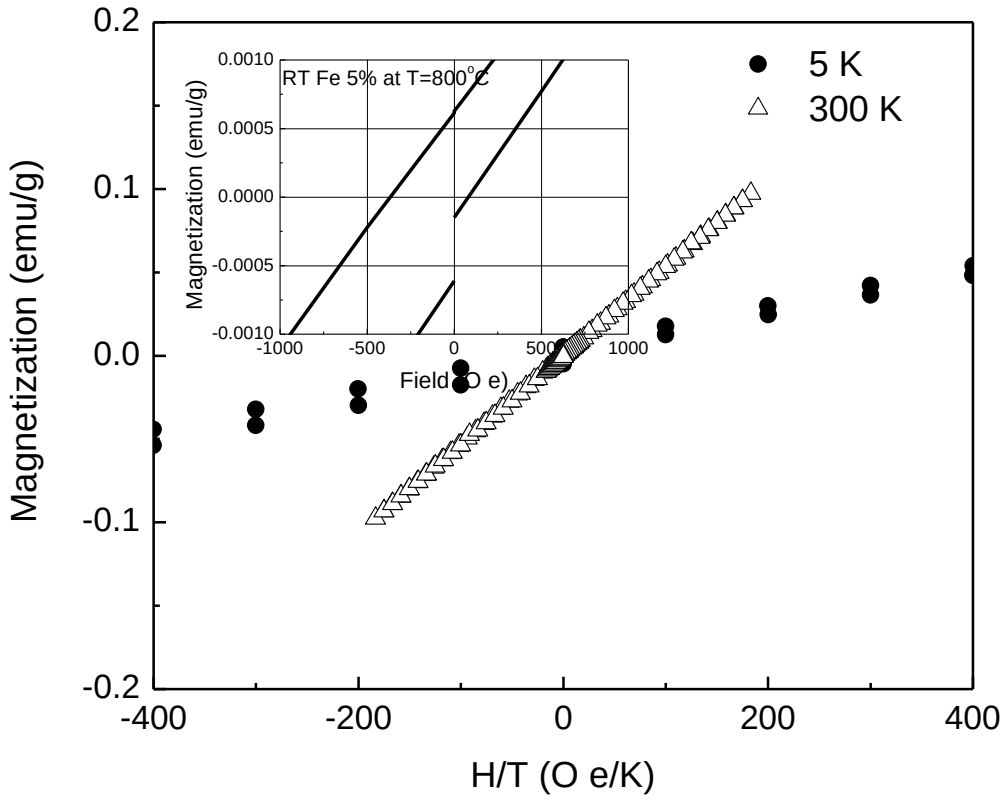
0.2
0.1
0.0
-0.1
-0.2
-400
-200
0
200
400
Magnetization (emu/g)
H/T (O e/K)
5 K
300 K
RT Fe 5% at T=800°C
0.0010
0.0005
0.0000
-0.0005
-0.0010
-1000
-500
0
500
1000
Magnetization (emu/g)
Field (O e)

Figure 10

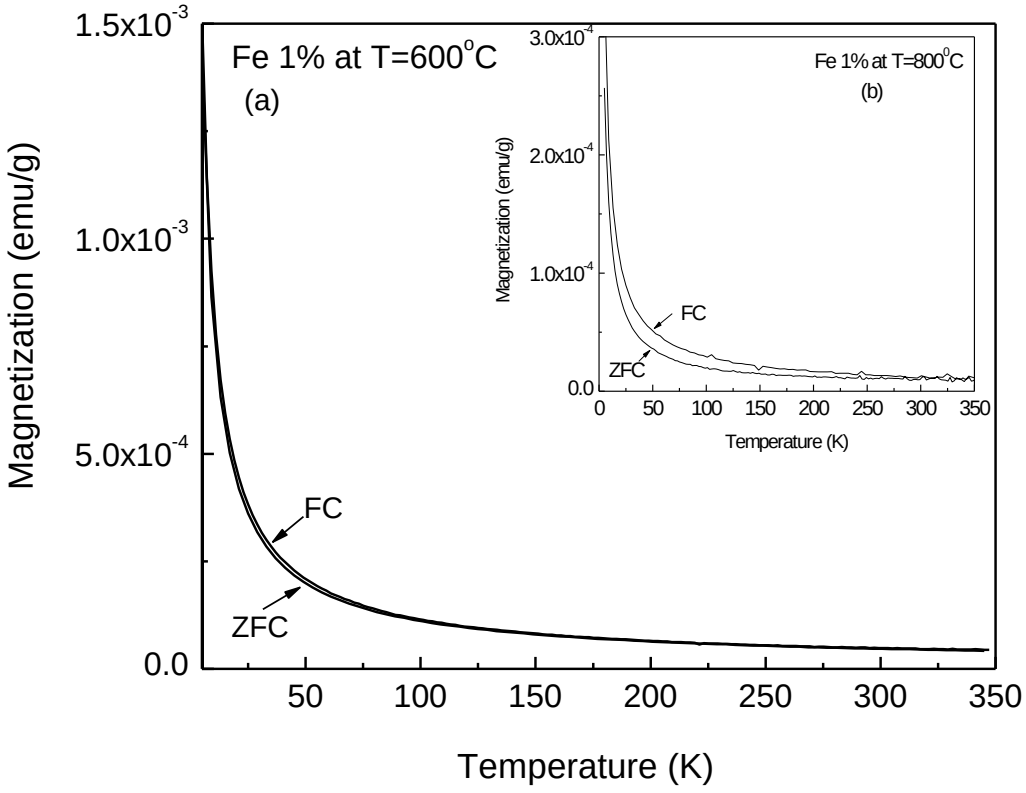
Fe 1% at T=600°C
(a)
Magnetization (emu/g)
1.5x10-3
1.0x10-3
5.0x10-4
0.0
FC
ZFC
50
100
150
200
250
300
350
Temperature (K)
Fe 1% at T=800°C
(b)
Magnetization (emu/g)
3.0x10-4
2.0x10-4
1.0x10-4
0.0
FC
ZFC
0
50
100
150
200
250
300
350
Temperature (K)

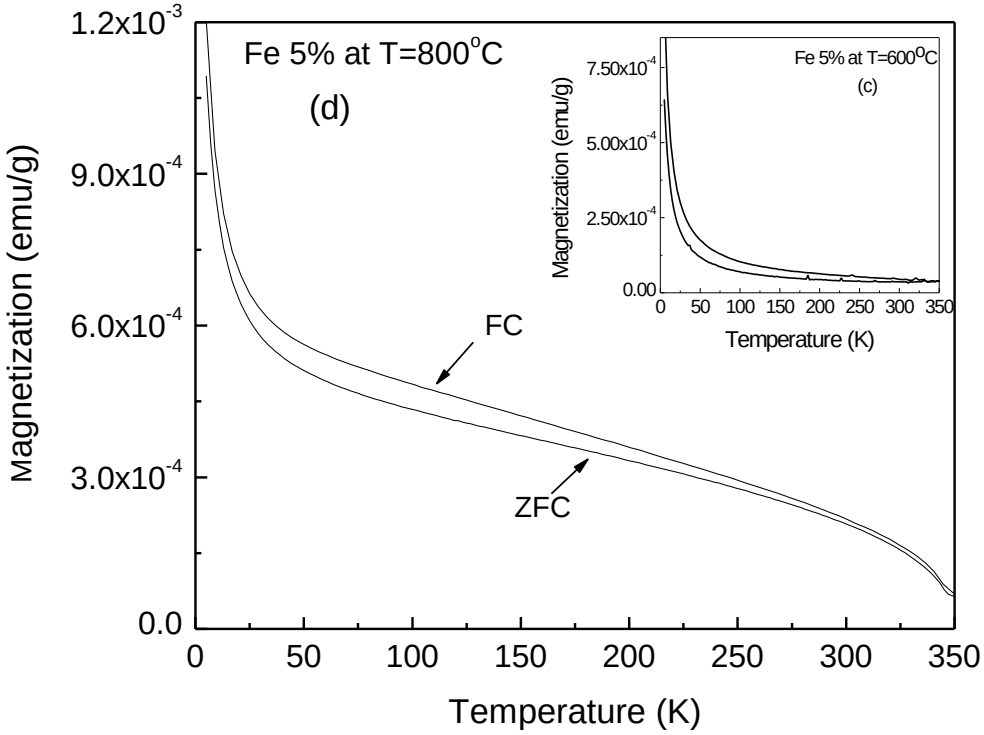
Fe 5% at T=800°C
(d)
FC
ZFC
Magnetization (emu/g)
Temperature (K)
1.2x10-3
9.0x10-4
6.0x10-4
3.0x10-4
0.0
0
50
100
150
200
250
300
350
Fe 5% at T=600°C
(c)
7.50x10-4
5.00x10-4
2.50x10-4
0.00

Figure 11

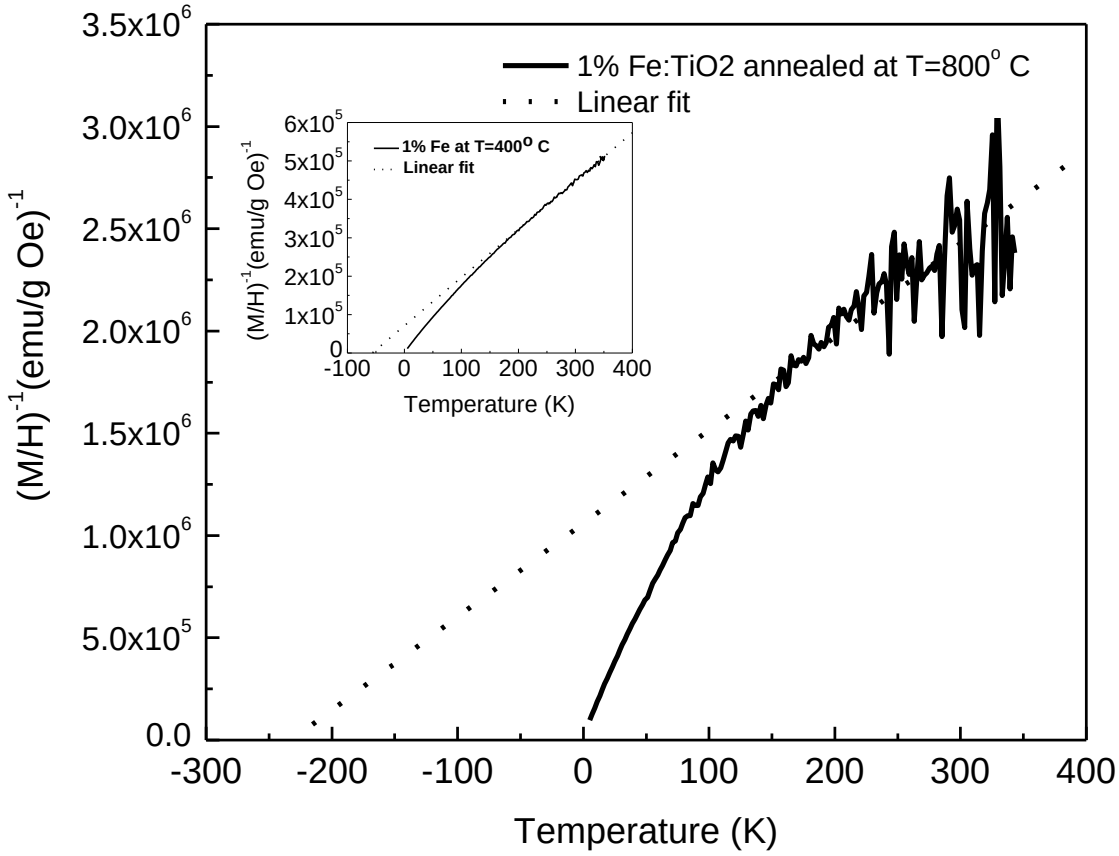
1% Fe:TiO2 annealed at T=800° C
Linear fit
(M/H)-1(emu/g Oe)-1
Temperature (K)
1% Fe at T=400° C
Linear fit
(M/H)-1(emu/g Oe)-1
Temperature (K)

(a)

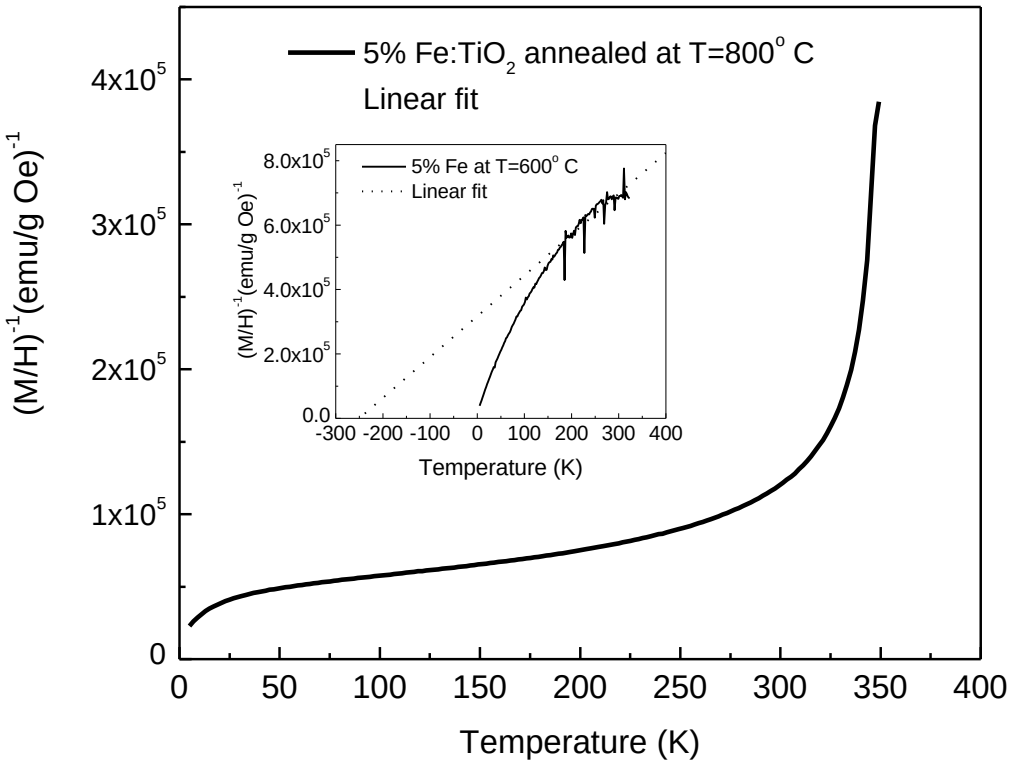
5% Fe:TiO2 annealed at T=800° C
Linear fit
(M/H)-1(emu/g Oe)-1
Temperature (K)
5% Fe at T=600° C
Linear fit
(M/H)-1(emu/g Oe)-1
Temperature (K)

(b)

Figure 12

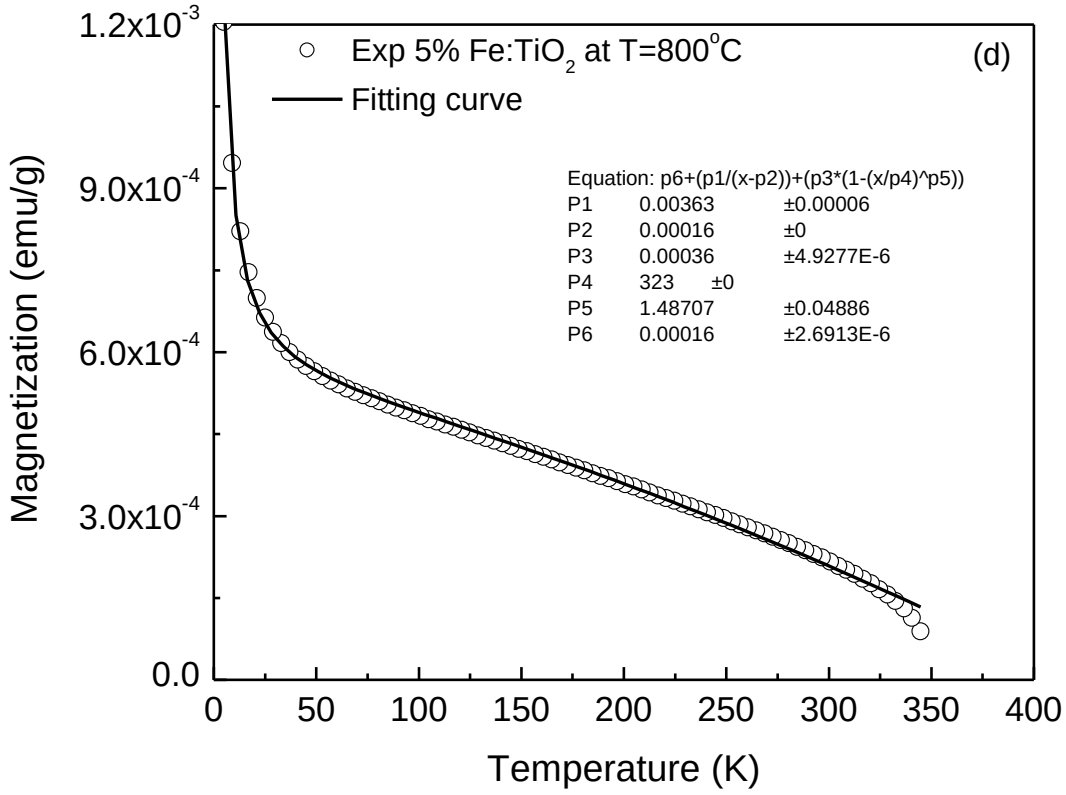
Exp 5% Fe:TiO2 at T=800°C
(d)
Fitting curve
Equation: p6+(p1/(x-p2))+(p3*(1-(x/p4)^p5))
P1 0.00363 ±0.00006
P2 0.00016 ±0
P3 0.00036 ±4.9277E-6
P4 323 ±0
P5 1.48707 ±0.04886
P6 0.00016 ±2.6913E-6
Magnetization (emu/g)
1.2x10-3
9.0x10-4
6.0x10-4
3.0x10-4
0.0
0
50
100
150
200
250
300
350
400
Temperature (K)